RESEARCH ARTICLE

Mechanisms of Pacific Summer Water variability in the Arctic's Central Canada Basin

M.-L. Timmermans[1], A. Proshutinsky[2], E. Golubeva[3], J. M. Jackson[4], R. Krishfield[2], M. McCall[1], G. Platov[3], J. Toole[2], W. Williams[5], T. Kikuchi[6], and S. Nishino[6]

[1]Department of Geology and Geophysics, Yale University, New Haven, Connecticut, USA, [2]Woods Hole Oceanographic Institution, Woods Hole, Massachusetts, USA, [3]Institute of Computational Mathematics and Mathematical Geophysics, Siberian Branch of Russian Academy of Sciences, Novosibirsk, Russia, [4]ASL Environmental Sciences, Inc., Victoria, British Columbia, Canada, [5]Fisheries and Oceans Canada, Institute of Ocean Sciences, Sidney, British Columbia, Canada, [6]Japan Agency for Marine Science and Technology, Yokosuka, Japan

Abstract Pacific Water flows northward through Bering Strait and penetrates the Arctic Ocean halocline throughout the Canadian Basin sector of the Arctic. In summer, Pacific Summer Water (PSW) is modified by surface buoyancy fluxes and mixing as it crosses the shallow Chukchi Sea before entering the deep ocean. Measurements from Ice-Tethered Profilers, moorings, and hydrographic surveys between 2003 and 2013 reveal spatial and temporal variability in the PSW component of the halocline in the Central Canada Basin with increasing trends in integrated heat and freshwater content, a consequence of PSW layer thickening as well as layer freshening and warming. It is shown here how properties in the Chukchi Sea in summer control the temperature-salinity properties of PSW in the interior by subduction at isopycnals that outcrop in the Chukchi Sea. Results of an ocean model, forced by idealized winds, provide support to the mechanism of surface ocean Ekman transport convergence maintaining PSW ventilation of the halocline.

1. Introduction

Water from the Pacific Ocean that flows northward through Bering Strait has important relationships to Arctic sea ice, ecosystems, and climate, by providing a source of nutrients, heat, and freshwater to the Arctic Ocean [*Coachman and Barnes*, 1961]. Although the flow pattern of Pacific Water is complicated as it transits the shallow Chukchi Sea, there are believed to be three main branches of the Bering Strait inflow: a westernmost branch through Herald Canyon, an eastern-most branch through Barrow Canyon, and flow over the central shelf in between [see, e.g., *Coachman and Barnes*, 1961; *Coachman et al.*, 1975; *Proshutinsky*, 1986; *Winsor and Chapman*, 2004; *Weingartner et al.*, 2005; *Woodgate et al.*, 2005; *Spall*, 2007; *Pickart et al.*, 2009] (Figure 1a). The modification of Pacific Water within the Chukchi Sea by surface buoyancy fluxes has strong seasonal and interannual variability that depends on ice cover and atmospheric conditions. Pacific Summer Water is Pacific-origin water that is modified in the Chukchi Sea during the summer, while the cooler, saltier Pacific Winter Water has its properties set in the Chukchi Sea in winter [*Coachman and Barnes*, 1961].

Pacific Water extends horizontally over most of the Canadian Basin sector (and thus spans a large fraction of the Arctic Ocean as a whole) [*Woodgate et al.*, 2010]. The relatively fresh layers resulting from Pacific inflows are important for the maintenance of the Arctic sea ice cover due to their role in insulating the overlying surface layers (in contact with sea ice) from deep Atlantic Layer heat [see *Carmack and Melling*, 2011]. However, Pacific Summer Water (PSW) also acts as a heat source and has itself been inferred to induce summer ice melt [*Fedorova and Yankina*, 1963; *Shimada et al.*, 2006; *Woodgate et al.*, 2010]. For example, *Woodgate et al.* [2010] assert that the Bering Strait inflow can initiate sea-ice melting through ice-albedo feedback (i.e., initial ice melt by warm Pacific Water at the surface leads to increased open water, which can absorb more incoming solar radiation, which can melt more ice). However, over the abyssal plain of the Canada Basin, *Toole et al.* [2010] show that PSW may be largely insulated from the surface ocean by the strong salinity stratification now present. Pacific Water makes up a significant fraction of the halocline in the Canada Basin and largely controls halocline stability and heat and freshwater storage. Our focus in this paper is to investigate characteristics and variability of PSW over the period 2003–2013 in the Central Canada Basin (CCB; defined here as the region within 79°N, 150°W, 74°N, and 135°W, Figures 1a and 1b) and to
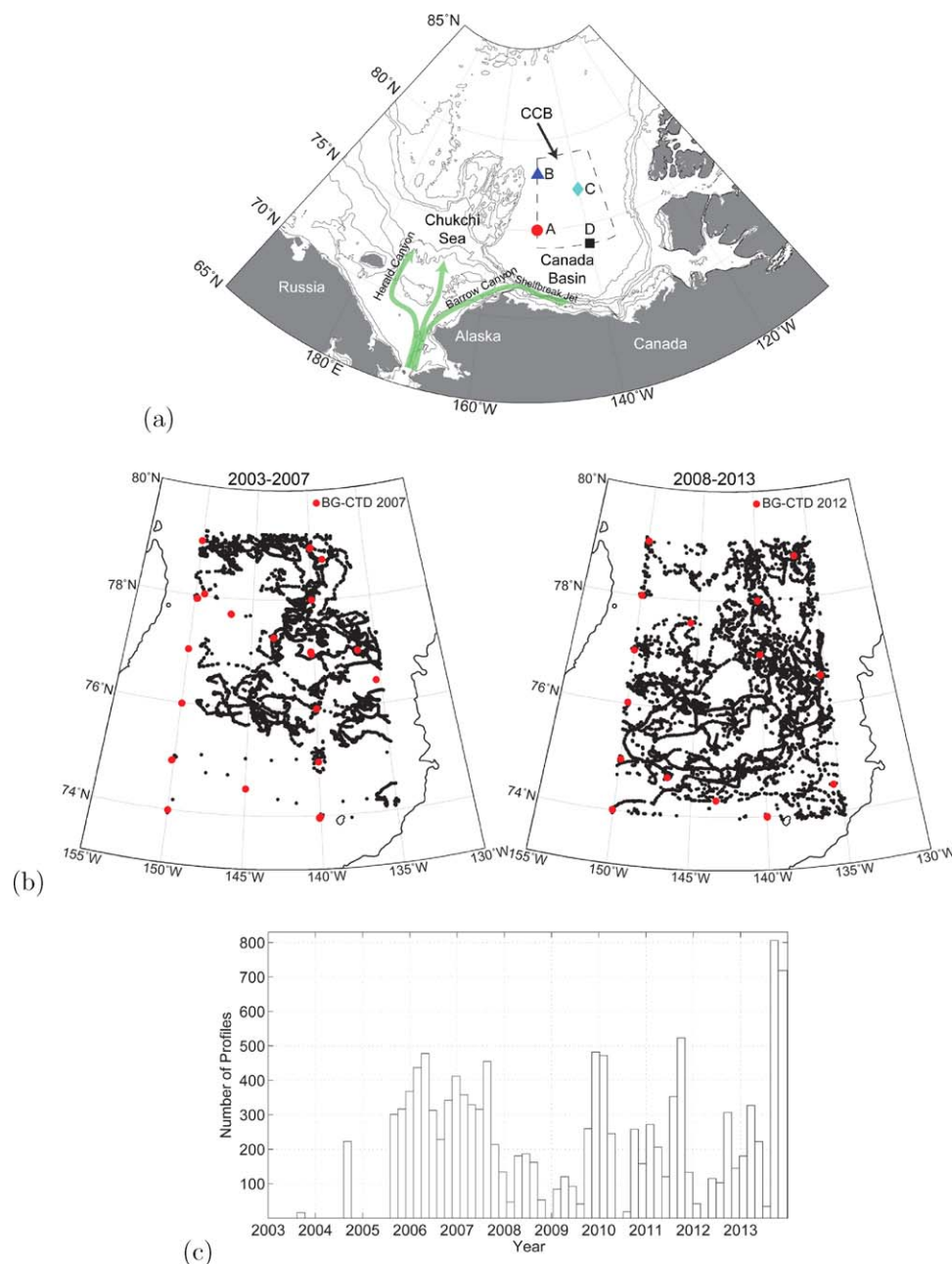
Figure 1. (a) Map of the Central Canada Basin (CCB) bounded by dashed lines within 79°N, 150°W, 74°N, and 135°W. Symbols show BGOS moorings A, B, C, and D. The 20, 40, 60, 100, 500, 1000, and 2000 m isobaths are plotted, and arrows show schematic pathways of Pacific Water inflow. (b) Maps showing ITP and BG CTD profile locations in the CCB: a total of 11,810 profiles between August 2003 and December 2013. Red dots indicate BG CTD profile locations for the years shown; in each year, the BG hydrographic profiles had a similar distribution in the CCB. (c) Number of profiles (ITP and BG CTD) in the CCB (bin size: 60 days).

place these in context with water mass transformations and mechanisms that transport Pacific Water to these regions.

The large-scale ice and ocean circulation in the Canada Basin is dominated by the anticyclonic Beaufort Gyre (BG). The BG is approximately centered over the CCB, with some interannual variability in location due to shifts in the center of the large-scale anticyclonic atmospheric circulation [*Proshutinsky et al.*, 2009]. There are three distinct layers that typically feature in waters shallower than PSW in the CCB. The surface mixed layer, with an average depth of 16 m in the summer and 24 m in the winter [*Toole et al.*, 2010], overlies the near-surface temperature maximum (NSTM)—a warm layer whose heat, derived from incoming summer
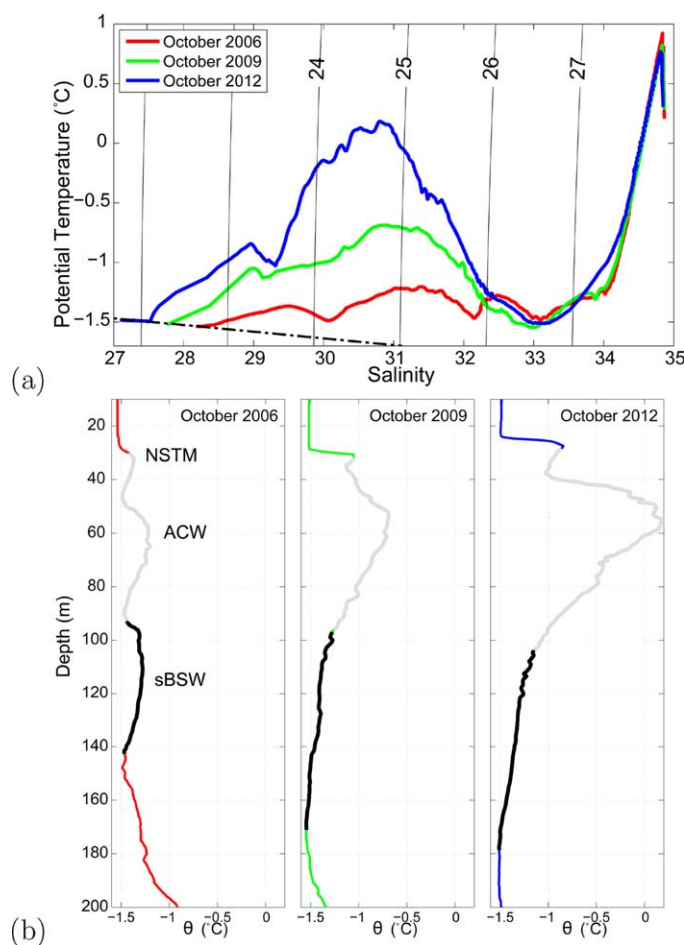
Figure 2. (a) Typical potential temperature (θ, [°C]) versus salinity (S) profiles from the CCB (around 78°N, 140°W) in October 2006, 2009, and 2012. Contours indicate potential density anomaly (kg m^{-3}) referenced to the surface (densities vary primarily in accordance with the salinities); the dashed line is the freezing line at 0 dbar. (b) Profiles of potential temperature corresponding to the curves in Figure 2a. The gray and black portions of the profiles mark the salinity ranges found here to be appropriate for the ACW ($29 < S \le 32.2$) and sBSW ($32.2 < S \le 33$), respectively. Notice in the latter 2 years, the absence of a maximal temperature in the salinity range of sBSW.

solar radiation, is trapped by stratification after sea ice melt [e.g., *McPhee et al.*, 1998; *Perovich et al.*, 2008; *Jackson et al.*, 2010]. The NSTM is often observed to overlie a weakly stratified remnant Winter Mixed Layer (rWML), a residual from the previous winter's mixed layer after seasonal restratification. The core of the PSW lies below these three layers, between ∼40 and 100 m deep in the Canada Basin [*Steele et al.*, 2004].

The salinities of the Pacific water masses are typically used to distinguish them from one another and from the NSTM (see Figure 2). The seasonally warmed PSW may be subdivided into Alaskan Coastal Water (ACW), originating (as the name indicates) from the Alaskan coast, and saltier (and typically, cooler) summer Bering Sea Water (sBSW) thought to originate in the Gulf of Anadyr [*Coachman et al.*, 1975]. The salinity range of ACW is typically taken to be $31 < S < 32$, while that of sBSW is taken to be $32 < S < 33$. The temperature maxima within these respective ranges are considered to be tracers for ACW and sBSW [*Shimada et al.*, 2001; *Steele et al.*, 2004] (Figure 2). Here we show some amendment to these traditional salinity bounds is required given PSW change in recent years. In addition to its distinct signature in temperature-salinity space, Pacific Water is characterized by low dissolved-oxygen (DO) content [e.g., *Falkner et al.*, 2005], presumably because of respiratory activity and nutrient regeneration; *Coachman et al.* [1975] note that oxygen utilization rates in the near-bottom water in the Chukchi Sea appear to be extremely high. Marked DO minima in the Canada Basin are found in the salinity range of the sBSW [*Timmermans et al.*, 2010].

Although much is still unknown of flow pathways and dynamics of PSW entering the Canada Basin interior, PSW properties in the interior Canada Basin bear some relationship to Pacific Water inflows to the Arctic. Mooring data indicate increased Pacific water transport through Bering Strait over the period 2001–2011, from about 0.7 Sv in 2001 to 1.1 Sv in 2011; this is associated with increased temperature and freshwater transports [*Woodgate et al.*, 2012; see also *Clement Kinney et al.*, 2014]. *Woodgate et al.* [2012] conclude that these increases in Bering Strait inflow resulted from an increased Pacific-Arctic pressure head; temperature transport increases were also attributed in part to warmer Bering Sea source waters. *Woodgate et al.*'s mooring analysis did not include the warm, fresh, Alaskan Coastal Current in the upper ocean, and they point out that the freshwater fluxes (and variability) they compute are likely underestimates since they do not account for changes in the shallowest layers. It is unclear to what extent changing source waters are reflected in the interior CCB; this will depend in large measure on prevailing wind and sea-ice conditions in any given year.

North of Bering Strait, one flow characterization is that the sBSW component of PSW moves northward from Herald Canyon and the central Chukchi shelf into the northern Canada Basin while ACW flows primarily through Barrow Canyon and via the Pacific water boundary current in the Beaufort Sea (the Beaufort shelfbreak jet) to the southern Canada Basin (see *Steele et al.* [2004], although they point out that the pathways are likely to be much more complicated). *Steele et al.* [2004] relate interannual variations in the regional distribution of ACW and sBSW in the Canada Basin (in the 1990s) to the wind conditions associated with different phases of the Arctic Oscillation (AO) index [*Thompson and Wallace*, 1998]. They find ACW to be more prevalent in the southern Canada Basin, while sBSW is more commonly found in the northern Canada Basin, with a distinct geographical separation between the two during strongly positive AO years where the dominant sBSW pathway is via the Transpolar Drift Stream. In years characterized by a lower AO index, *Steele et al.* [2004] suggest reduced geographical separation of the PSW types as both the ACW and the sBSW are swept into a larger and stronger Beaufort Gyre. These large-scale flow patterns also modify the temperature and salinity of PSW in the surface ocean at the basin margins. *Kwok and Morison* [2011] show that the dynamic ocean topography pattern in 2008 suggests a surface circulation where shelf water, freshened by Eurasian river runoff, is carried eastward along the Russian coast, where it can freshen Pacific Waters at the surface. *Morison et al.* [2012] attribute freshwater content increases in the Pacific Water layers from 2005 to 2008 in the Canada Basin to this upper-ocean circulation pattern characterized by an increased AO Index. In this study, we will examine the mechanism by which Pacific Summer Water at the surface in the Chukchi Sea propagates to the interior Canada Basin where it resides at depth under the surface layers.

The flow patterns just described are in fact highly variable on time scales much shorter than interannual or seasonal. For example, *Pickart et al.* [2009] analyze the flow across the outer Chukchi shelf that originates from Herald Canyon. They find that when easterly winds are weak, there is strong eastward flow (in contrast to a direct northward flow consistent with Pacific water properties in the northern Canada Basin in some years, *Steele et al.* [2004]) and the canyon outflow feeds the Beaufort shelfbreak jet. Idealized barotropic model experiments support the hypothesis that northeasterly to easterly winds can reverse the eastward flow along the Beaufort shelf, and force Pacific Water along a more northerly pathway across the Chukchi Sea and into the interior Canada Basin [see *Winsor and Chapman*, 2004]. Consistent with this, *Nikolopoulos et al.* [2009] observe reversals to the west of the mean eastward flow of the shelfbreak jet during strong upwelling-favorable wind events. Further, *von Appen and Pickart* [2012] analyze mooring measurements (summers 2002–2004) to find there are two configurations for the Beaufort shelbreak jet: a surface-intensified ACW configuration and a bottom-intensified sBSW configuration (note that the latter authors refer to sBSW as Chukchi Summer Water). They show how in 2002–2004, the eastward extent of the PSW shelfbreak current is limited by active baroclinic instability and eddy formation; eddies have been shown to be an important mechanism for offshore transport of Pacific Water [see *Pickart et al.*, 2005; *Spall et al.*, 2008; *Watanabe*, 2011]. *von Appen and Pickart* [2012] estimate that the shelfbreak current can only transport the PSW about 150 km (for the sBSW configuration) to 300 km (for the ACW configuration) east of 152°W (i.e., PSW enters the Canada Basin interior west of about 145°W) before waters are lost to the formation of eddies.

Changes in Pacific Water flow patterns in recent years have been attributed to a general increase in easterly winds associated with a stronger Beaufort High and deeper Aleutian Low (E. T. Brugler et al., Seasonal to interannual variability of the Pacific water boundary current in the Beaufort Sea, submitted to *Progress in Oceanography*, 2014). Brugler et al. (submitted manuscript, 2014) analyze moored measurements across the Beaufort shelfbreak jet to show an 80% decrease in volume transport in the current (predominantly in the summer months) between 2002 and 2011. They propose that in recent years with stronger easterly winds, Pacific heat, and freshwater are being advected directly north into the Canada Basin interior instead of progressing eastward in the Beaufort shelfbreak jet.

Much remains to be understood about how changes to PSW source-water properties and circulation pathways, as well as modification of source water by mixing and surface buoyancy fluxes, are reflected in property changes in the interior Canada Basin. For the interior Canada Basin, *Jackson et al.* [2011] found that ACW freshened between 2004 and 2008. Specifically, they report that the portion of the water column between the rWML and ACW temperature maximum freshened from $30 < S < 32$ in 1993 to $28 < S < 32$ in 2008, and suggest that this change resulted from surface buoyancy fluxes and vertical mixing rather than from changing source waters or pathways. However, as they acknowledge, the 1-D diffusion model they

employ does not account for lateral advection, wind mixing, or the freeze-melt cycle. In fact, to reconcile the discrepancies in the salinity field between their 1-D model and observations, they suggest that accumulation of freshwater in the surface layers is also required (namely, freshening by sea-ice melt, river runoff, and changes in the wind-driven circulation).

In another recent study of PSW, *Bourgain and Gascard* [2012] examine the temperature maximum in the PSW range to show an increase by about 0.3°C between the periods 1997–2002 and 2007–2008 in the Canada Basin. In contrast to *Jackson et al.* [2011], they attribute this warming to changes in the Bering Strait inflows propagating into the basin, consistent with observations by *Woodgate et al.* [2010] of warmer Bering Strait inflows beginning in 2001. *Woodgate et al.* [2010] find monotonic increases in the temperatures of Bering Strait inflows from 1999 to 2007. *Bourgain and Gascard* [2012] note that the timing of the warmer Bering Strait influxes is consistent with the PSW signals they observe in the interior Canada Basin for advection speeds on the order of 1 cm s^{-1}. It is unclear in this scenario how PSW is advected to the interior.

Here we analyze the considerable number of temperature and salinity measurements from Ice-Tethered Profilers (ITPs, www.whoi.edu/itp) [*Toole et al.*, 2011; *Krishfield et al.*, 2008], Beaufort Gyre Observing System (BGOS, http://www.whoi.edu/beaufortgyre/) moorings, and US/Canada BGOS/Joint Ocean Ice Studies (JOIS) hydrographic surveys in the Central Canada Basin from 2003 through 2013 (Figure 1) to assess the recent variability of the Pacific Summer Water, and explore potential causes for this variability. We support our observational interpretation by employing a wind-forced Arctic Ocean model [see *Golubeva and Platov*, 2007]. The model is used to examine the transport of Pacific Water after it enters the Arctic Ocean both in the presence of a large-scale anticyclonic wind forcing and in the absence of winds. Measurements are described in the next section where we further examine the different components of PSW identified by the presence of potential temperature maxima, θ_{max}, within specified salinity ranges; we show how the proper choice of these salinity ranges is vital for the accurate identification of these water masses and for the characterization of their evolution. In section 3.1, we quantify the interannual variability in both the salinity and temperature of ACW θ_{max} (we find relatively little change from year to year in properties of the deeper sBSW θ_{max}), as well as PSW freshwater and heat content. In section 3.2, we examine spatial patterns of PSW in the CCB. Section 4 presents a dynamical interpretation for the observed PSW variability in the CCB, including calculations of wind-forced Ekman pumping (section 4.2), and examination of idealized model experiments (section 4.3). Results are discussed and summarized in section 5.

2. Measurements and Methods

2.1. ITP and BGOS Measurements

Extensive ITP data, collected between September 2004 and December 2013, are analyzed here. ITPs are automated profiling systems that are deployed in multiyear ice floes and sample the properties of the underlying ice-covered ocean for periods of up to 3 years [*Krishfield et al.*, 2008; *Toole et al.*, 2011]. Each system consists of a surface buoy, which sits on top of the ice with a tether extending through the ice into the ocean to a depth of about 750 m. An underwater profiling instrument cycles vertically up and down this tether, collecting temperature and salinity profiles and transmitting data via satellite to shore in near-real time. The ITP incorporates a Sea-Bird 41-CP CTD; conductivity data are adjusted for consistency with recent ship observations from the region. The conductivity calibration involves the derivation of profile-dependent multiplicative adjustments to match ITP potential conductivities on deep potential temperature surfaces (below the Atlantic Water core) to spatially varying reference fields produced with ship-based CTD data. The resulting ITP salinity data match the ship data to better than 0.005. For several of the later years of ITP data analyzed here, no adjustments were applied to the conductivity data; in these cases, profiles that show offsets in deep salinity values were excluded. On the basis of postdeployment calibration of three recovered ITPs, temperature and pressure sensor accuracies were found to be ±0.001°C and ± dbar, respectively. Detailed processing procedures are outlined at http://www.whoi.edu/itp. The high temporal and spatial resolution of ITPs enables a detailed assessment of the water mass structure. The entire ITP system drifts with the ice floe; for typical ice drift speeds of about 10–20 cm/s, a horizontal survey resolution of roughly 3 km is obtained for profiles collected every 8–12 h.

The ITP system numbers relevant to the Central Canada Basin (CCB, Figure 1), operating between September 2004 and December 2013, are the following: 1–6, 8, 13, 18, 21, 32-3, 34, 35, 41-3, 52-5, 62, 64-5, and

68–70. The CCB is the focus of our study because it had the densest data coverage in the deep Arctic (11,810 quality profiles between 2004 and 2013) from which the most reliable trends could be determined (Figures 1b and 1c). Furthermore, considering interannual shifts in the center of the Beaufort Gyre (see *Proshutinsky et al.* [2009], with updates in *Proshutinsky et al.* [2011, 2012]), one can argue that this region encompasses the Beaufort Gyre center for each year studied [see also *McPhee*, 2013].

We also analyze measurements from the four BGOS moorings, each with a McLane Moored Profiler (MMP) that measures conductivity, temperature, depth (plus the two components of horizontal velocity, although variations in the PSW flow field are too weak to be reliably resolved by the velocity sensors) operating since 2003 in the Canada Basin (see *Proshutinsky et al.* [2009], for further details), denoted by the letters shown in Figure 1. MMP profiles are alternately separated by 6 and 48 h, spanning an approximate depth range of 50–2000 m. The shallow limit of this depth range precludes examination of the uppermost Pacific waters; however, we will show here that inferences can be made about the ACW through an examination of the sBSW at each of the four mooring sites. Accuracy of the final processed MMP salinity data is better than 0.005 [*Proshutinsky et al.*, 2009]. In addition to the mooring measurements, we use CTD data collected under the US/Canada BGOS/JOIS projects (http://www.whoi.edu/beaufortgyre). Standard hydrographic sites revisited annually (during August to October) enable investigation of PSW properties covering most of the CCB region every year since 2003. Additional CTD measurements in the Chukchi Sea were obtained from hydrography archived at the 2013 World Ocean Database (WOD13; www.nodc.noaa.gov/OC5/WOD13/) and surveys of the R/V Mirai (Japan Agency for Marine-Earth Science and Technology, JAMSTEC) in 2012 and 2013.

2.2. Methods

For each potential temperature (θ)/salinity (S) profile in the CCB, we characterize ACW and sBSW by the maximum potential temperature θ_{max} in their respective salinity ranges, which we will determine in this section. Curvature maxima (peaks) are found in the salinity ranges specified to ensure temperature maxima associated with the boundaries of the range are not mistaken for θ_{max} of the water mass in question. Our procedure to determine these maxima is as follows. We begin by computing the warmest temperature peak that satisfies $S < 33$ and is deeper than 40 m, where this depth will be justified later in this section. A PDF of this PSW θ_{max} (Figure 3a) shows a multimodal structure, with one mode centered around $S \approx 32.6$ (salinity of sBSW θ_{max}), and others (salinity of ACW θ_{max}) in the salinity range $S \approx 30.7$ to $S \approx 31.7$. This clustering of θ_{max} salinities in combination with visual inspection of individual profiles, suggests a salinity of 32.2 is the appropriate boundary between ACW and sBSW for this data set. Yearly histograms (Figure 3b) show that between 2004 and 2006 some profiles exhibited a sBSW θ_{max} that was warmer than the ACW θ_{max}. In later years, either a cooler sBSW θ_{max} was observed, or it was absent entirely.

While we have delineated the ACW/sBSW boundary, it remains to ensure differentiation of the ACW θ_{max} from the NSTM. To this end, for each profile, we find the shallowest temperature peak in the upper 40 m, and the warmest temperature peak deeper than 40 m that satisfies $S < 32.2$ (the ACW θ_{max}). A shallow θ_{max} (likely a NSTM) is only selected where it is found beneath a homogeneous surface layer. We identify two clusters in a plot of these θ_{max} values versus the corresponding salinity for (1) the shallowest temperature peak in the upper 40 m and (2) the warmest temperature peak that is deeper than 40 m with $S < 32.2$ (Figure 4). This demonstrates a clear delineation between the NSTM and the ACW θ_{max}. (Note that we found the technique of seeking a temperature minima, associated with the rWML, at a depth between the NSTM and the ACW θ_{max} to differentiate the water masses could not be used for much of the year when the NSTM did not exist.) The clear delineation between the NSTM and ACW suggests that each water type can be defined by salinity. From 2003 to 2013 in the CCB, no ACW θ_{max} is found to be fresher than $S = 29$. Visual individual inspection of profiles where no ACW θ_{max} is found reveals that less than 5% of ACW θ_{max} are not identified by our algorithm because they are shallower than 40 m; the NSTM is always shallower than 40 m in the data set analyzed here. Note that *Bourgain and Gascard* [2012] require that the temperature maximum that defines PSW be deeper than 40 m, stating that this ensures differentiation from the NSTM.

In summary, we characterize ACW by the range $29 < S < 32.2$, with the θ_{max} deeper than 40 m (to ensure differentiation from the NSTM, with the understanding that fewer than 5% of profiles for which ACW θ_{max} are shallower than 40 m will be excluded from the analysis) and sBSW by the range $32.2 < S < 33$. In some years, the fresh bound on ACW ($S = 29$) will encompass the NSTM (e.g., Figure 2), while in other years, an
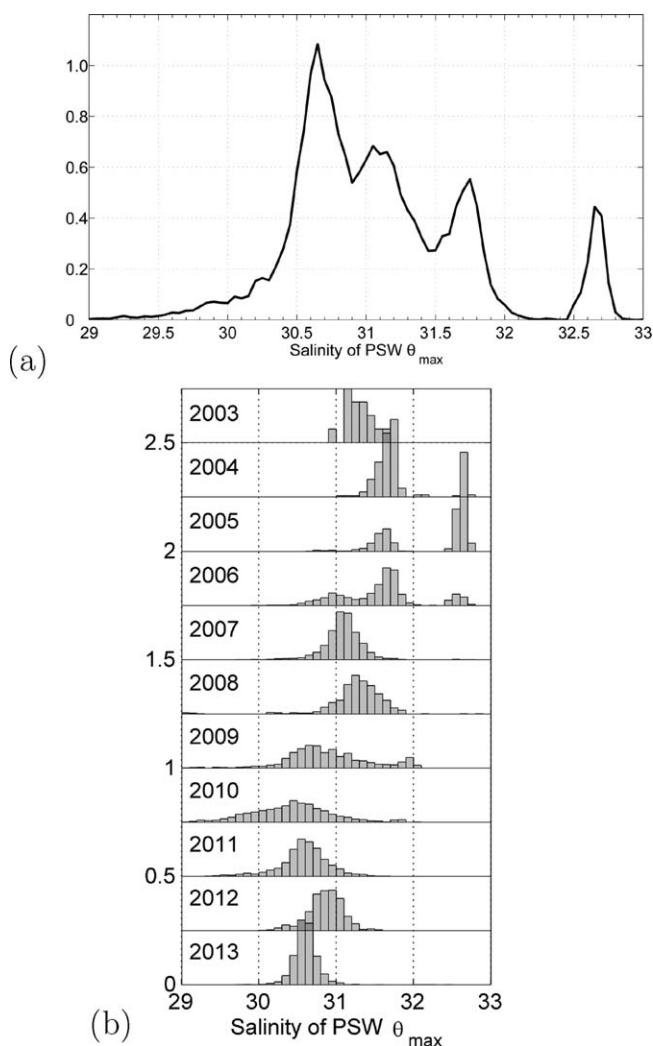
Figure 3. (a) PDF of the salinity of the θ_{max} for $S < 33$ and deeper than 40 m for all CTD and ITP profiles (2003–2013) in the CCB. A binsize of 0.05 is used in the calculation. (b) Yearly histograms of the salinity of the θ_{max}. Binsize is 0.1 and number in each bin is divided by the total number of observations in a given year. Each year is offset on the y axis by 0.25.
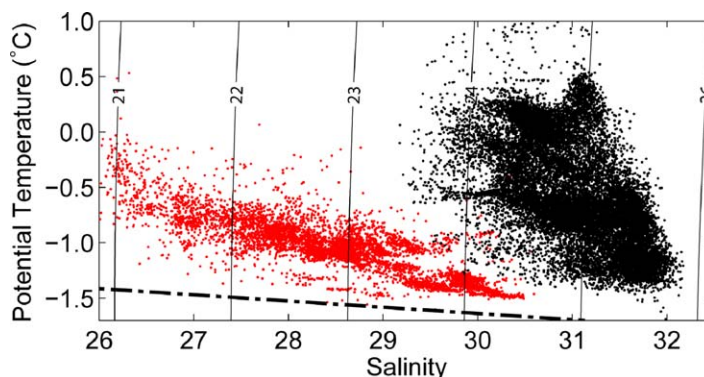

Figure 4. Potential temperature versus salinity plot of θ_{max} and corresponding salinity (for all CTD and ITP profiles [2003–2013] in the CCB) where the red dots indicate the shallowest temperature peak in the upper 40 m and the black dots indicate the warmest temperature peak that is deeper than 40 m with $S < 32.2$. The two clusters show a clear delineation between the NSTM (red dots) and the ACW θ_{max} (black dots).

ACW θ_{max} with a salinity close to this value is observed. To assess interannual variability of integrated freshwater and heat content of PSW, a saltier shallow bound must be considered so that the seasonally varying NSTM layer does not influence the results. Our analysis of the BGOS mooring data only includes an assessment of the deeper portion of PSW; the freshest salinities measured by the moorings are typically greater than $S \approx 30$ because the moorings sample no shallower than about 50 m below the ice-ocean interface.

It is of note that within the ACW salinity range $29 < S < 32.2$, two local temperature maxima are sometimes present. A second cooler local temperature maximum is occasionally observed in the range $31 \leq S \leq 32$ in the same profiles that indicate temperature maxima in the range $30 \leq S \leq 31$ (e.g., Figure 5). *Jackson et al.* [2011] attribute this double peak to an intrusion of cold water (possibly shelf water; see *Shimada et al.* [2001]) on the ACW temperature maximum in 2006, and show how the presence of two peaks in the ACW salinity range is most common in 2009. For the years and region studied here, the double-peak feature appears with no apparent seasonal or spatial bias. It appears in all years except 2003–2004, where it could be that a double peak was not observed because data coverage was not as extensive in those years. In each year for which a double peak is observed, it shows up only in a few percent of profiles, except in 2009, when a double peak is observed in about 8% of profiles. The feature does not appear to be
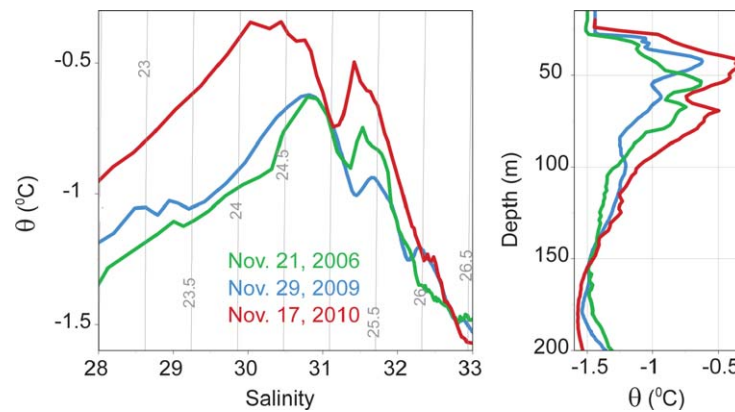
Figure 5. (left) Potential temperature versus salinity in the CCB for the dates shown. Contours indicate potential density anomaly (kg m^{-3}) referenced to the surface. Two temperature peaks can be seen in the salinity range of the ACW ($29 < S < 32.2$). Cooler sBSW peaks are present (before 2009) around a salinity of 32.4. (right) The corresponding potential temperature profiles showing the two peaks (in the ACW salinity range) in each profile between around 45 and 65 m depth.

temporally stable or laterally coherent, but rather is an intermittent feature in space and time. In some cases, the double peak can be attributed to a cold-core anticyclonic eddy rather than an intrusive layer, although existing data are insufficient for a detailed assessment. In 2011, multiple shallower halocline temperature peaks are associated with eddies of the same class as those analyzed by *Timmermans et al.* [2008].

3. Changing Characteristics of PSW

Having determined appropriate salinity ranges for the constituent water masses of PSW, it is possible to investigate the evolution of their properties over the study period, assuming temporal changes dominate spatial variability of PSW in the CCB. Spatial variability within the CCB, inferred from the large spread in PSW characteristics in the CCB in some years, will also be examined.

3.1. Temporal Variability

Salinity of the ACW θ_{max} in the CCB shows a general freshening trend from 2003 to 2013. Before 2009, the ACW θ_{max} lay predominantly within the conventional range of $31 < S < 32$ considered by *Steele et al.* [2004] and others; a distinct freshening to $S \approx 30.5$ of the ACW θ_{max} occurred in 2010 (Figure 6). Freshening and warming of the ACW θ_{max} are broadly related. The ACW θ_{max} shows a general warming temperature trend, with considerable interannual variability (Figure 6). *Bourgain and Gascard* [2012] reported a warming of about 0.3°C in the temperature maximum in the salinity range $31 < S < 33$ between the periods 1997–2002 and 2007–2008 in the Canada Basin. We find rather larger variability than this from year to year in the CCB between 2003 and 2013 (Figure 6a). The depth of the ACW θ_{max} is in the range 40–90 m (with a mean and standard deviation of 60 ± 10 m) in the CCB for the years examined (Figure 6c); this depth range is not appreciably different from that found by *Steele et al.* [2004]. Fresher ACW θ_{max} are generally related to shallower ACW θ_{max}.

Spatial variability (discussed in the next section) in the ACW θ_{max} properties over the CCB contributes to the large spread in values observed in some years; after 2008, relatively smaller spatial variability is observed. Importantly, the BG CTD data (with uniform spatial sampling distributions from year to year) show essentially the same temporal variability as the ITP data, indicating that the variable spatial distribution of available ITP profiles during any given month do not appear to bias the overall results.

There does not appear to be significant seasonal variability in properties of the CCB ACW θ_{max}. Seasonal variability is limited to shallower layers, as evident in time series of layer-averaged temperature in the upper 40 m compared to the 40–70 m depths (Figure 7).

In contrast to the ACW θ_{max}, properties of the sBSW θ_{max} vary little over the analysis period (not shown), with mean (and standard deviation) sBSW θ_{max} around -1.2 ± 0.1°C (i.e., sBSW is typically traced by a cooler θ_{max} than ACW) and salinity of the θ_{max} around 32.6. The sBSW θ_{max} is found at depths in the range 85–160 m (with a mean and standard deviation of 120 ± 14 m). One key feature of the sBSW θ_{max} is that it
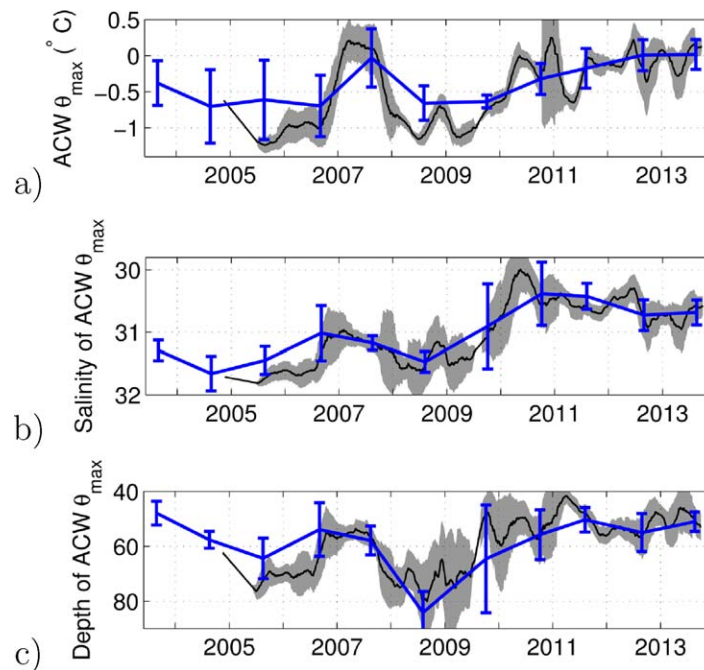
Figure 6. (a) ACW θ_{max} (°C), (b) salinity of ACW θ_{max}, and (c) depth (m) of ACW θ_{max} in the CCB. Tick marks on the x axis represent 1 January of each year. ITP data are shown by the black lines: 60 day running means are plotted, and the shading represents one standard deviation. BG CTD data are shown in blue: mean values in a given year are plotted with bars indicating one standard deviation. In most years, CTD stations with an even distribution over the entire CCB (Figure 1) were occupied in the same month.

is only observed in the northern sector of the CCB [cf. *Steele et al.*, 2004] for the years studied here, and in the later years it is not observed at all in the CCB (see, for example, 2009 and 2012 profiles in Figure 2b, where there is no characteristic θ_{max} in the sBSW salinity range). We examine these spatial patterns in section 3.2.

While the ACW and sBSW θ_{max} (and corresponding salinity) are useful water mass tracers, their properties must not be equated with the water masses themselves. We next examine the evolving freshwater and heat content of PSW. As noted above, the complicating influence of the strongly seasonally varying NSTM and surface layer are introduced if the freshwater content is calculated over a depth range that includes the fresher end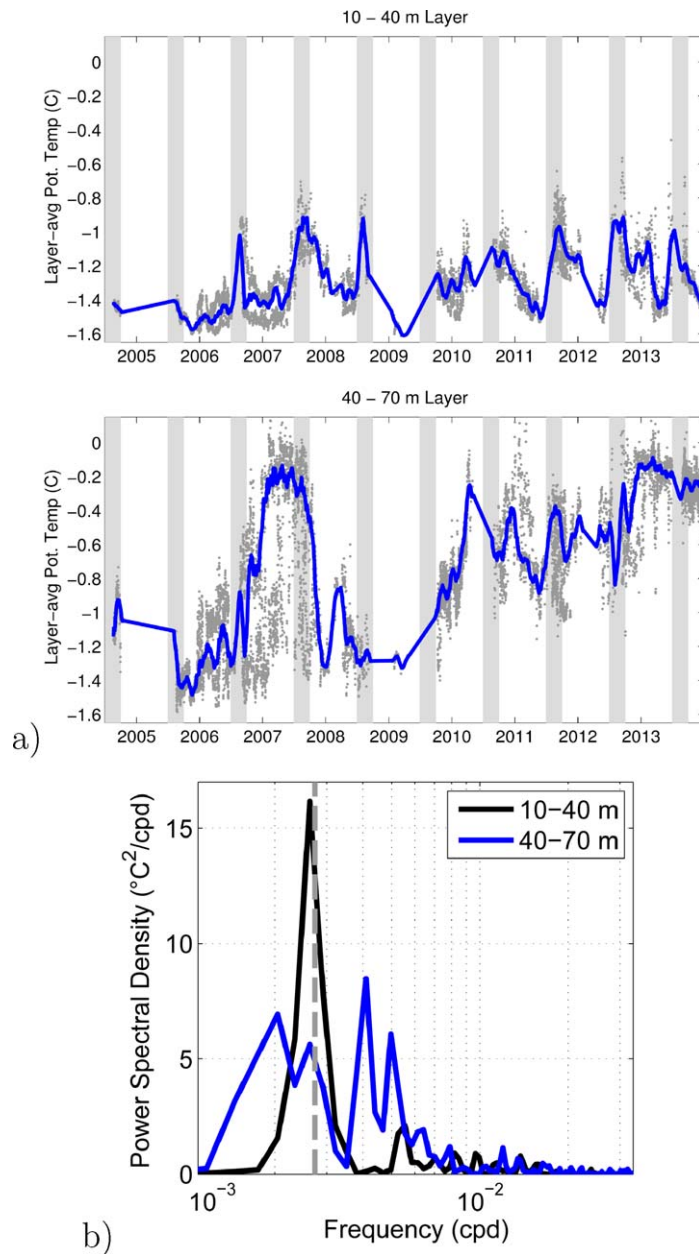 of the ACW salinity range (see Figure 7). Therefore, we examine the integrated freshwater content (relative to a salinity of 33) in the range $31 < S < 33$ (Figure 8a). This is defined as

$$FW_{PSW} = \int_{d(S=31)}^{d(S=33)} \frac{33-S}{33} dz = h_{PSW}\left(1 - \frac{\bar{S}_{PSW}}{33}\right), \tag{1}$$

where $d(S=33)$ is depth of the 33 isohaline [and similar for $d(S=31)$], h_{PSW} is the thickness of the layer bounded by the 31 and 33 isohalines, and $\bar{S}_{PSW}$ is the layer-averaged salinity. As we saw for the evolution of the salinity of the ACW θ_{max}, a marked freshening trend is apparent. The two time series (Figures 6b and 8a) are significantly correlated; the correlation coefficient is $r = -0.65$. Likewise, temporal change in integrated heat content of the $31 < S < 33$ layer relative to freezing temperature (Figure 8b) is statistically significantly correlated with the ACW θ_{max} ($r = 0.80$). Layer-averaged temperature and salinity of the $31 < S < 33$ layer are also well correlated to ACW θ_{max} and salinity of ACW θ_{max}, respectively. Again, the ship based CTD data are in agreement with the ITP data that are more irregularly distributed in a comparable temporal window.

Freshwater and heat content in the range $31 < S < 33$ were also calculated at each of the four BGOS moorings: A, B, C, and D. Positive trends of freshwater and heat content from moorings B and C generally follow those of the spatially distributed ITP and hydrographic data (Figure 8, symbols). Moorings A and D (in the southern portion of the CCB, Figure 1) show relatively higher freshwater and heat content in the early part of the record (through 2007) than the northern moorings B and C. From 2008 to 2013, the freshwater and heat contents were similar at all moorings. These results indicate that there was a spatial shift in the properties of PSW over the study period.

While freshwater and heat content time series show correlations with the salinity and temperature (respectively) of ACW θ_{max} (and layer-averaged salinity and temperature), the evolution of layer thickness is important (Figure 9). Between 2003 and 2010, the thickness of the $31 < S < 33$ layer increased from about 90 m to about 120 m. This thickness increase is due to a deepening of the $S = 33$ isohaline, with relatively smaller change in the $S = 31$ isohaline which showed a modest deepening through 2008 and a slight shoaling thereafter. The total thickness of the $31 < S < 33$ layer increased between 2003 and 2013. The deepening

Figure 7. (a) Layer-averaged temperature (°C) between (top) 10–40 m and (bottom) 40–70 m from all ITP profiles in the CCB; waters shallower than 10 m are not included given a typical shallow bound of 7 m for ITP sampling. Blue lines show the running mean over 30 days, and the gray shaded bars indicate July-August-September. (b) Frequency spectra for the temperature time series shown in the plots above. A dominant seasonal signal is clear in the 10–40 m temperature.

of the deep isohaline is a manifestation of the intensification of the Beaufort Gyre circulation [*Proshutinsky et al.*, 2009], and this contributes to thickening of the PSW layer (because the shallow isohaline does not deepen at the same rate) and overall increases in PSW freshwater.

The change in freshwater content, $\Delta FW_{PSW} = FW_{PSW}^{f} - FW_{PSW}^{i}$ (superscripts f and i denote final and initial, respectively), can be expressed as

$$\Delta FW_{PSW} = \left[FW_{PSW}^{i} \left(\frac{h_{PSW}^{f}}{h_{PSW}^{i}} - 1 \right) \right] + \left[FW_{PSW}^{f} - \frac{h_{PSW}^{f}}{h_{PSW}^{i}} FW_{PSW}^{i} \right], \qquad (2)$$
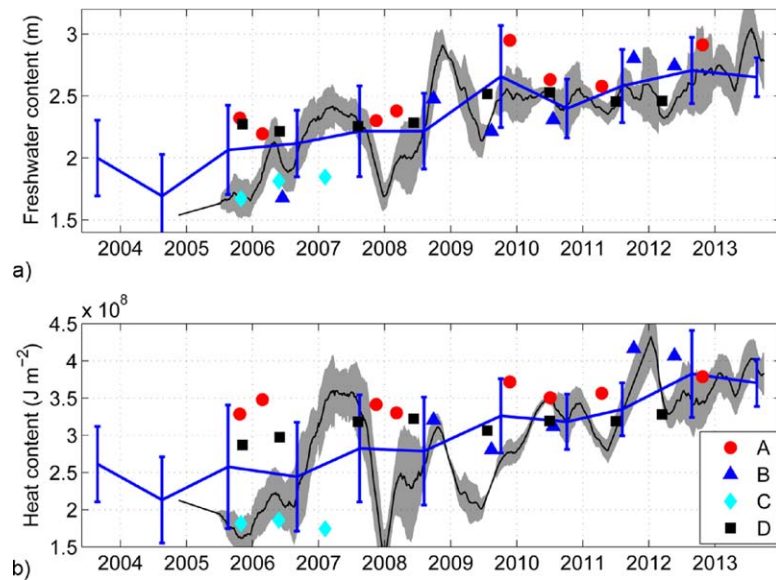
Figure 8. (a) Freshwater content (m) and (b) heat content (J m^{-2}) in the range $31 < S < 33$ in the CCB. Waters fresher than $S = 31$ are not considered as in early years, the NSTM lies at the fresh end of the salinity range that encompasses the ACW for all years. Freshwater content is calculated relative to a reference salinity of 33. Heat content is calculated relative to freezing temperature. BG CTD data are shown in blue: mean values in a given year are plotted with bars indicating one standard deviation. ITP data are shown by the black lines: 60 day running means are plotted, and the shading represents one standard deviation. Mean values from each of the four BGOS mooring A, B, C (2003–2008), and D deployments are shown by the symbols (each symbol is plotted at the mean date for which MMP profiles were obtained during the yearly deployments).
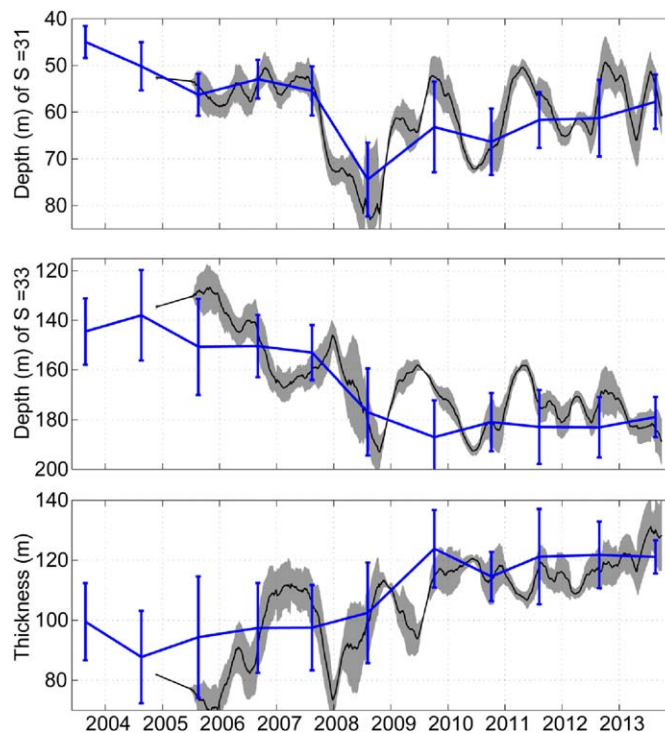

Figure 9. Depth (m) of the (top) $S = 31$ and (middle) $S = 33$ isohalines, and (bottom) thickness of the layer defined by $31 \leq S \leq 33$ in the CCB. BG CTD data are shown in blue: mean values in a given year are plotted with bars indicating one standard deviation. ITP data are shown by the black lines: 60 day means are plotted, and the shading represents one standard deviation.

the sum of the contribution due to the change in layer thickness, $h^f_{PSW} - h^i_{PSW}$, [first term] plus the contribution due to salinity change [second term]. We estimate that between 2003 and 2013, 63% of the freshwater content increase is a result of layer thickness increase, while 37% of the increase is due to layer freshening.

Similar to the properties of the ACW θ_{max}, there is no strong seasonal signal in freshwater and heat content in the range $31 < S < 33$. This is demonstrated in an example depth-time section showing the interannual variability of temperature and salinity, and time series of freshwater and heat content at mooring D (Figure 10). While in winter there is some indication of increased Ekman pumping (due to strengthened anticyclonic wind stress curl;
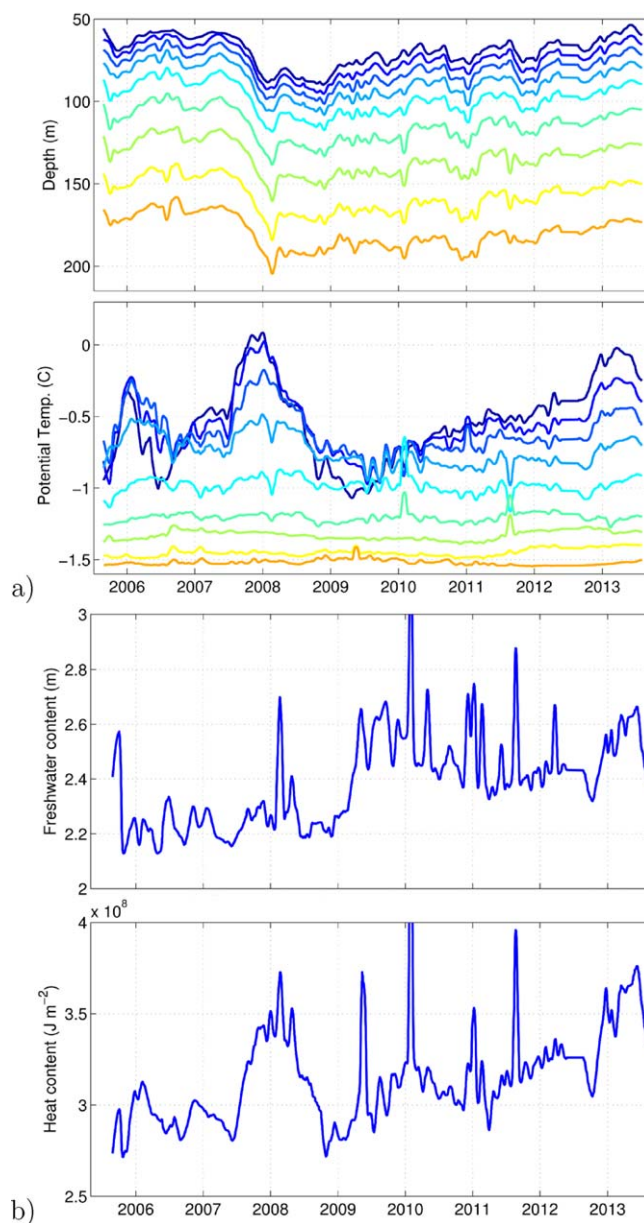
Figure 10. (a) Top: mooring D (75°N, 140°W) depth of selected isohalines $S = 31$ to 33, with spacing of 0.25. Bottom: potential temperature (°C) on isohalines shown in the top plot. Mooring D was only deployed starting in 2005. Seasonal variability of isohaline depths is related to intensified wind-stress curl in winter with no apparent seasonal variability in temperature on these isohalines. (b) Freshwater content (m) (top) relative to $S = 33$ and heat content (J m^{-2}) calculated relative to freezing temperature in the range $31 < S < 33$; 30 day running averages are plotted. Narrow peaks and troughs can be attributed to mesoscale eddies; values for the two peaks that extend beyond the plot ranges are 3.2 m (top) and 4.5×10^8 J m^{-2} (bottom).

e.g., *Proshutinsky et al.* [2009], see their Figures 5 and 6), causing isopycnal/isohaline deepening, there is no apparent seasonal variability in temperature on isohalines relevant to the ACW. Numerous mesoscale eddies manifest as short-time scale perturbations [see, e.g., *Carpenter and Timmermans*, 2012] in the history of integrated freshwater and heat content.

3.2. Spatial Variability of PSW in the CCB

While there is a clear interannual signal in properties of PSW, freshwater and heat content, for a given temporal window, we attribute the standard deviation in the estimates to spatial variability in the properties over the CCB. This spatial variability is evident in maps of freshwater and heat content (Figure 11). It is understood that heat and freshwater content variability approximately follow temperature and salinity of the ACW θ_{max}. The maps show a clear gradient in heat and freshwater from lower values in the southwest to higher in the northeast, in addition to the overall increase in heat and freshwater content over the past decade in the region.

To examine the spatial property gradients in detail, it is instructive to analyze the drift of ITP 6 between 1 September 2006 and 31 August 2007. Over this period the ITP drifted along an approximately North to South path (around 78.6°N to 74.8°N) in the vicinity of 140°W (Figures 11a and 12). This ITP had a dissolved-oxygen (DO) sensor in addition to the standard CTD (see *Timmermans et al.* [2010] for details,
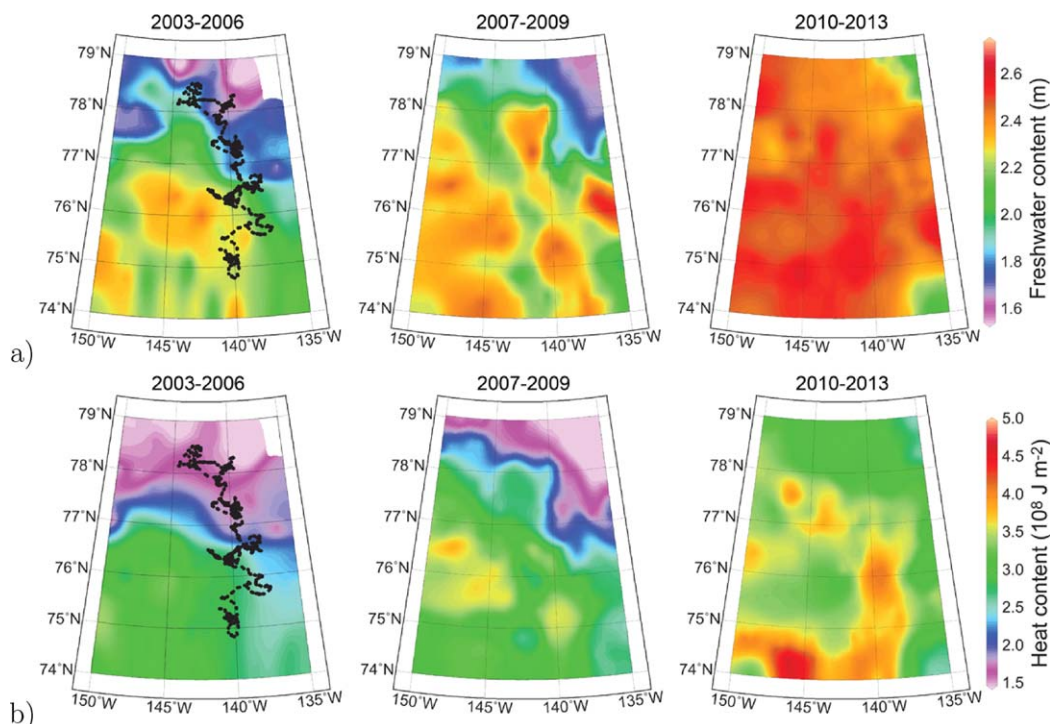
including data processing). DO measurements may be used as another tracer of the constituent water masses of PSW; sBSW is associated with anomalously low DO. Around 76.5°N–77°N, the ITP crossed a distinct lateral change in water mass properties (Figure 12) between a cool ACW $\theta_{max}(\approx -1°C$ at $S \approx 31)$ to the north and a markedly warmer ACW θ_{max} ($>0°C$ at $S \approx 31$) to the south (Figure 11 marks this change with respect to heat and freshwater content). Associated with this transition in vertical temperature-salinity structure of the water column is a clear temperature maximum in the salinity range of the sBSW (on $S \approx 32.5$) and a corresponding very low dissolved oxygen in the north, while on the south side of the front there is no sBSW θ_{max} (Figure 12b). This may appear to be temporal variability as the ITP drift spanned about

Figure 11. (a) Maps of freshwater content (m) and (b) heat content (J m^{-2}) in the range $31 < S < 33$ in the CCB for the years shown. Freshwater content is calculated relative to a reference salinity of 33, and heat content is calculated relative to freezing temperature. The profile locations of ITP 6 between 1 September 2006 and 31 August 2007 are shown on the 2003–2006 period maps.

1 year; however, the drift track of the ITP is faster than the temporal variability in properties. Evidence from the localized moorings, as well as the effectively synoptic BG CTD stations spanning the entire CCB, confirms this.

Potential temperature versus salinity plots in the region of $\theta-S$ space for sBSW from the four BGOS moorings show the presence of an sBSW θ_{max} only in the two northernmost moorings. Furthermore, the northernmost moorings, B and C, show the disappearance of the sBSW θ_{max} starting in 2006 (mooring B) and 2007 (mooring C) (Figure 13), consistent with the north-eastward progression of the water mass boundary (Figure 11). It would appear that the water mass structure that in 2013 occupies the full CCB (in an areal sense), and can be distinguished by the absence of sBSW θ_{max}, is related to spatial shifts in water masses spanning the full depth of the halocline (<200 m), coupled with warming and freshening.

To summarize, results from ITP and CTD profiles from 2003 to 2013 show that the ACW θ_{max} warmed and freshened, and did not show any apparent seasonal variability. Our analysis distinguishes PSW from the seasonally varying overlying layers. Properties of the ACW θ_{max} are correlated with changes in layer-averaged temperature and salinity for the layer defined by $31 < S < 33$. Over our study period, freshwater content increase in the PSW layer is due both to layer thickness increase, and freshening of the layer. A lateral transition in water mass properties characterized by a cooler ACW and a prominent sBSW θ_{max} to the north and warmer ACW with no apparent sBSW θ_{max} to the south was observed around 77°N–78°N in the CCB from 2003 to 2009. The transition appears to have shifted northeastward in recent years, which have seen overall increases in PSW temperature, heat and freshwater content averaged over the CCB.

4. What Drives PSW Changes in the CCB?

Here we show how Ekman transport convergence/divergence driving Ekman pumping in the Chukchi Sea, coupled with general freshening and warming there, can explain the observed PSW changes in the CCB. Several driving factors (reviewed in section 1) have been discussed with respect to Pacific Water variability in the Canada Basin. It is clear that in situ mixing, changes in source-water properties, shifting wind patterns, and changes in the strength of the large-scale wind forcing all influence PSW properties in the CCB. It is
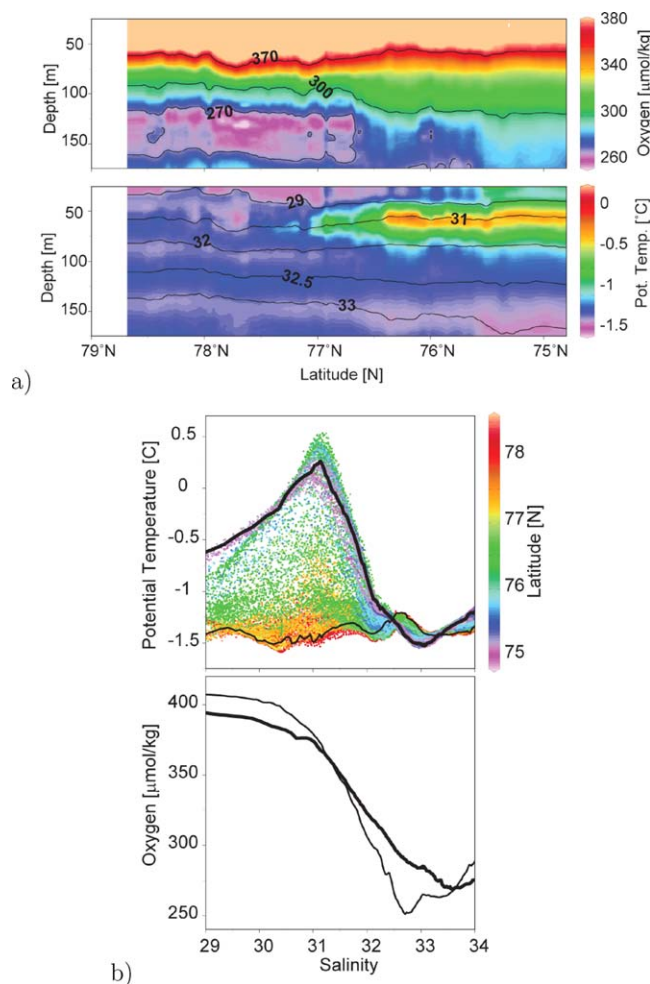
Figure 12. (a) North-South section (along approximately 140°W) of dissolved oxygen (top) and potential temperature (bottom) measured by ITP 6 between 1 September 2006 and 31 August 2007 (Figure 11); selected salinity contours are overlaid in the bottom plot. Note that oxygen % saturation shows essentially the same patterns as oxygen. (b) Top: potential temperature versus salinity from ITP 6 over the same time as in Figure 12a. Bottom: dissolved oxygen versus salinity from one of the northermost profiles in the top plot (thin black line) and one of the southernmost (thick black line). The sBSW is traced by a local minimum in DO (and a temperature maximum).

essential, however, to understand the processes which bring PSW to the CCB if we are to identify the most probable mechanisms behind the PSW variability (most notably its warming and freshening in recent years). These transport processes are our focus here, beginning with a discussion of water property gradients between the Chukchi Sea and the interior Canada Basin.

In the Chukchi Sea, PSW properties are set by surface heat fluxes and net precipitation, properties of Pacific Water inflow through Bering Strait, as well as eastward directed surface flows from the coast of Siberia [see, e.g., *Morison et al.*, 2012]. *Newton et al.* [2013] analyze oxygen isotope ratios and nutrient concentrations to show that PSW in the Beaufort Gyre consists of a mixture of about 85% Pacific inflow water and about 15% surface Chukchi/East Siberian Sea water. In the Chukchi Sea region in summer and early fall, measurements show salinity contours in the PSW range outcrop, and those surface waters have temperature and salinity properties that relate directly to the PSW layer in the interior Canada Basin (Figure 14). In winter, surface properties in the Chukchi Sea resemble the saltier, colder Pacific Winter Water. In all seasons there is a front in the vicinity of the Chukchi slope between the inflowing Pacific Water and the relatively fresh Beaufort Gyre surface water.
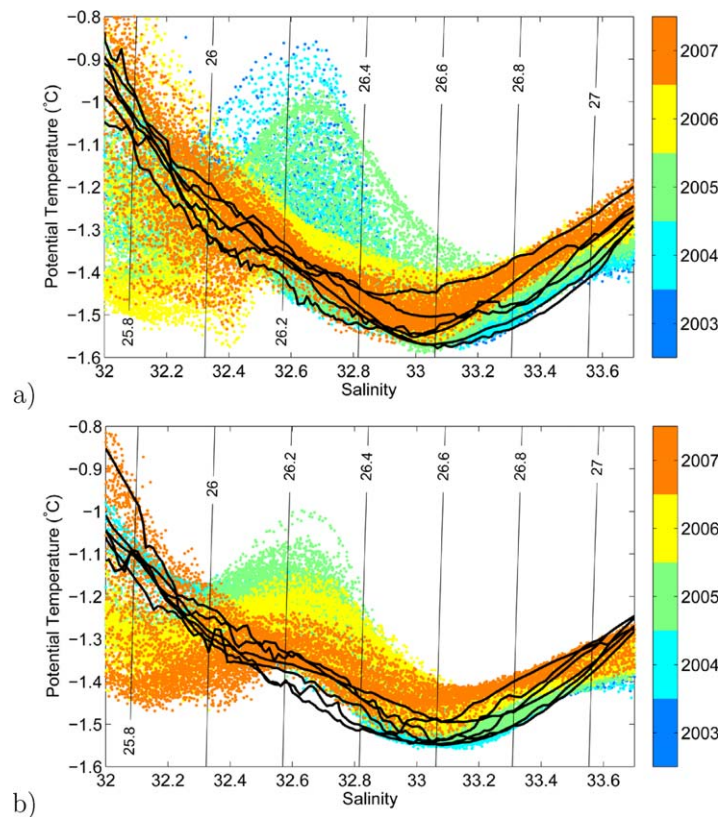
The typical surface water structure is a lateral gradient in surface salinity from high salinity in the Chukchi Sea to low salinity in the CCB [i.e., the Beaufort Gyre freshwater center] (Figure 14, and see, e.g., *Timmermans et al.* [2014], their Figure 5.16). Example September salinity sections off the Chukchi shelf slope and into the deep basin show outcropping isopycnals in the PSW salinity ranges to the south (Figures 15a and 16a). The northern extensions of the transects are characterized by thinner mixed layers and increased stratification compared to the Chukchi Sea. An important feature is that lateral gradients in surface temperature-salinity values approximately map on to vertical profiles in the deep basin (Figures 15b and 16b). This mapping structure is consistent with water being transferred from the surface in the Chukchi Sea into the halocline below and thereafter isolated from the direct effects of wind stress. The temperature-salinity mapping suggests that properties at the surface in the Chukchi Sea set the temperature-salinity properties in the interior where there is relatively weak property modification by mixing; warm PSW can be traced to the deep basin in the section shown in Figure 16. Of course, at further distances from the source region (e.g., the CCB), maximum PSW temperatures are lower than their source waters due to small lateral and vertical diffusion, but we expect the trends in surface Chukchi Sea properties to be reflected in PSW property trends in the interior.

Figure 13. Potential temperature (θ, [°C]) versus salinity (S) plots in the region of $\theta - S$ space for sBSW from (a) mooring B and (b) mooring C. Black lines are BG CTD profiles at each of the mooring sites taken in fall in each year from 2008 to 2013; the entire measurement records from moorings A and D (beginning in 2003 and 2005, respectively) lie in the range of the black profiles shown in each plot (i.e., no sBSW θ_{max} is observed at these mooring sites). Labeled contours indicate potential density anomaly (kg m^{-3}) referenced to the surface.

4.1. Subduction

The flux of water (originating at surface-outcropping isopycnals) into the halocline is quantified by a subduction rate, defined as the vertical velocity of a water parcel with respect to the base of the mixed layer [see *Iselin*, 1939; *Woods*, 1985; *Marshall*, 1997]. For a steady mixed layer of depth *h*, subduction (on an *f* plane) is given by

$$Su = -w_e + \mathbf{u_h} \cdot \nabla h, \qquad (3)$$

where w_e is Ekman pumping velocity (negative downward) determined from wind and sea-ice stresses at the ocean surface, $\mathbf{u_h}$ is the horizontal velocity of a water parcel at the base of the mixed layer where positive *Su* represents subduction (Figure 17). The second term accounts for the lateral transport of fluid from the base of a deep mixed layer to below a shallower mixed layer over some horizontal distance (i.e., lateral induction). Subduction given by equation (3) will be enhanced by an eddy-induced transport, expected to be significant in baroclinically unstable regions with strongly sloping isopycnals [e.g., *Marshall*, 1997; *Spall et al.*, 2008; *Thomas*, 2008].

In the mid to high-latitude ice-free oceans, the transfer of fluid from the surface to the pycnocline occurs over wind-driven gyres and in frontal regions. Thermocline ventilation takes place by subduction in regions
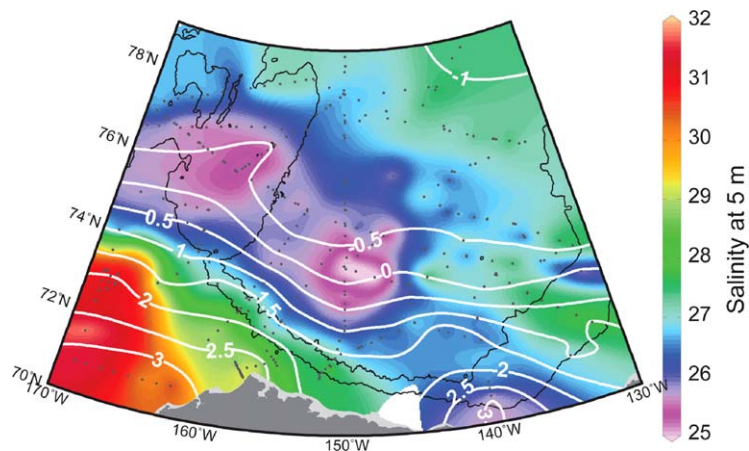

Figure 14. Map of salinity at 5 m depth from BGOS/JOIS and Mirai expeditions in August/September 2012 and 2013; white contours indicate potential temperature (°C) at 5 m depth and black dots mark profile locations. The 500 and 2500 m isobaths are shown.
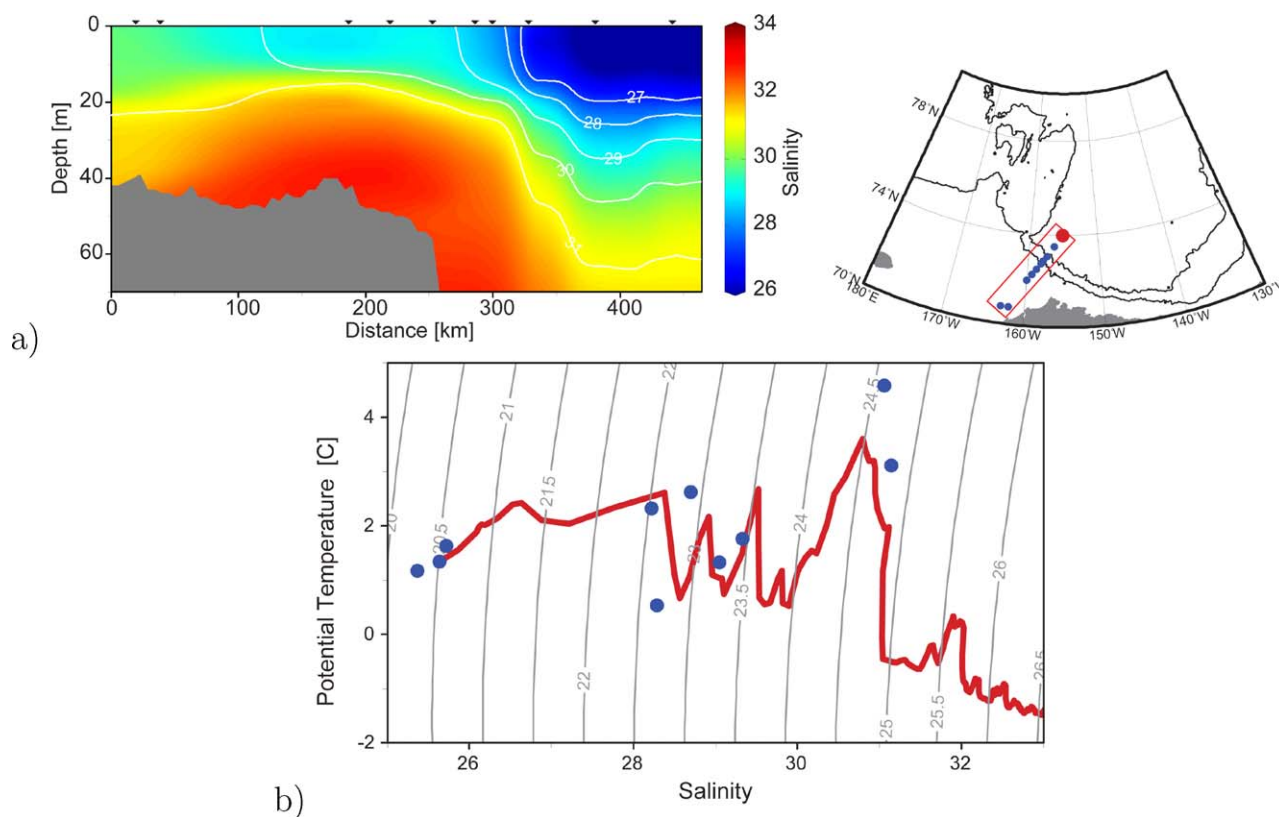
Figure 15. (a) Salinity section in September 2012 (Mirai expedition) from (left) the Chukchi shelf/slope into (right) the Canada Basin as shown in the map. (b) Potential temperature versus salinity plot showing the northernmost profile (red line) in the map shown in Figure 15a; blue dots indicate surface potential temperature salinity values for the stations shown in the map, with values becoming fresher toward the north. Near-vertical gray lines are lines of constant potential density (with respect to the surface).

where water masses with thermocline properties outcrop at the surface [see, e.g., *Iselin*, 1939]. Waters in the mixed layer at the end of winter (when mixed layers reach their deepest and most dense as a result of intense cooling) are transferred to the permanent thermocline [e.g., *Stommel*, 1979; *Marshall*, 1997]. Below the mixed layer, water masses spread along isopycnals while being advected to greater depths as they are swept along geostrophic contours.

In the Chukchi Sea, the front at which subduction is believed to occur is maintained continuously by inflowing Pacific Water, and strengthened by the large-scale wind-driven circulation associated with the Arctic High. Analogous to the thermocline in midlatitudes, the properties of this strong salinity front have a significant impact on the structure and variability of the Canada Basin halocline. Many different processes influence the structure of these water masses and their seasonal and interannual variability: sea ice thermodynamics, concentration and modification of wind stress input to the ocean, complicated surface stress gradients in the marginal ice zone, variations in inflowing Pacific Water, buoyancy forcing and river input. In the following sections, we illustrate only the influence of large-scale wind forcing (anticyclonic flow centered on the Beaufort Gyre) in combination with inflowing Pacific Water to demonstrate the halocline ventilation processes suggested by the data, with the additional processes to be examined in a future study.

4.2. Ekman Pumping

Rates of Ekman pumping (vertical velocities associated with Ekman transport convergence/divergence) are estimated here accounting for both air-water and ice-water stresses following the methodology of *Yang* [2006, 2009]. Surface wind stress is derived from the geostrophic wind [see *Proshutinsky and Johnson*, 1997] computed using the National Center for Atmospheric Research-National Centers for Environmental Prediction (NCAR-NCEP) reanalysis sea-level pressure. Ice-ocean stress is derived from sea-ice drift data. Sea-ice motion vectors (through December 2012) are derived from multiple remote and in situ sources [*Fowler*
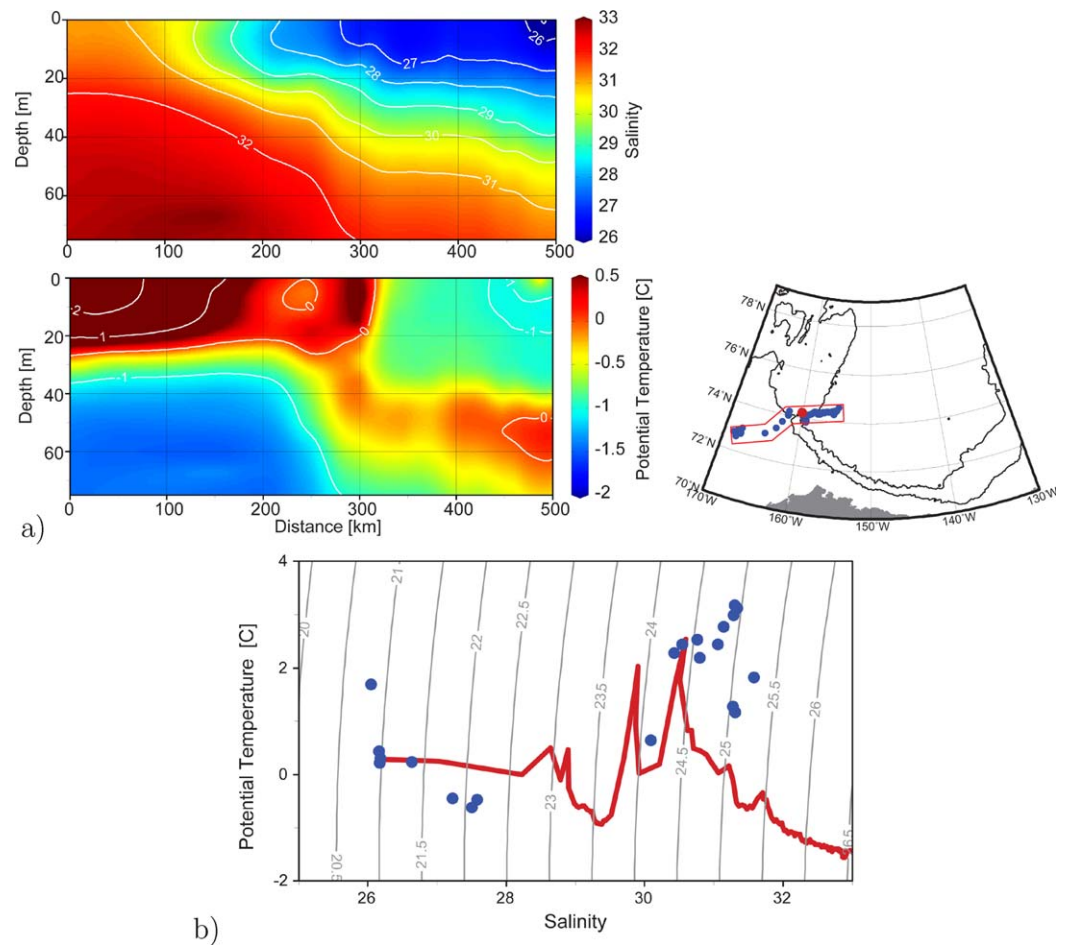
Figure 16. (a) Salinity/potential temperature (°C) sections in August/September 2013 (2013 Mirai expedition and ITP 64) from the (left) Chukchi shelf/slope into (right) the Canada Basin as shown in the map. (b) As in Figure 15b for the section shown in Figure 16a.

et al., 2013] and sea-ice concentration data were downloaded from the NSIDC. Monthly means were calculated based on daily data, and all variables were linearly interpolated to the same 25 km Equal-Area Scalable Earth Grid (EASE-Grid; www.nsidc.org). Total stre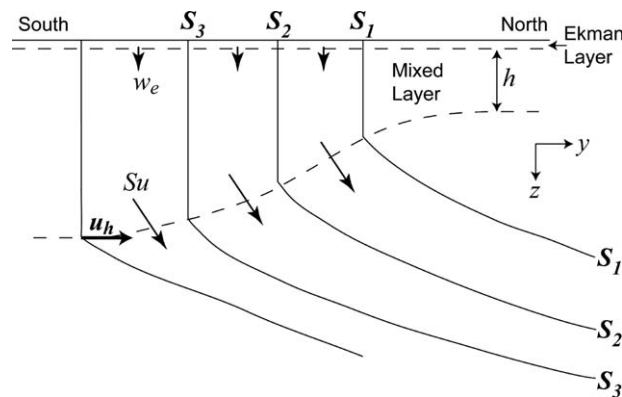ss curls were used to compute monthly mean distributions of Ekman downwelling and upwelling; full details are given in Yang [2006, 2009]. Note that this method does not take into account ocean geostrophic currents which, in addition to wind forcing, drive sea-ice motions. In summer, when wind forcing is typically weaker than in winter, there is likely some error induced by neglecting the ocean geostrophic flow; this is particularly true in frontal and boundary regions (and where ice cover is present) where geostrophic flows are strongest [see, e.g., McPhee, 2013]; however, the general patterns and magnitudes found here should remain the same.

Figure 17. Schematic showing isohalines (equivalently isopycnals) outcropping in the mixed layer [see Nurser and Marshall, 1991]. Ekman pumping velocity w_e (negative downward) is determined from wind and sea-ice stress fields, $\mathbf{u_h}$ is the horizontal velocity of a water parcel at the base of the mixed layer (shown as the dashed line), and the subduction rate Su is the mass flux per unit surface area through the mixed layer base.

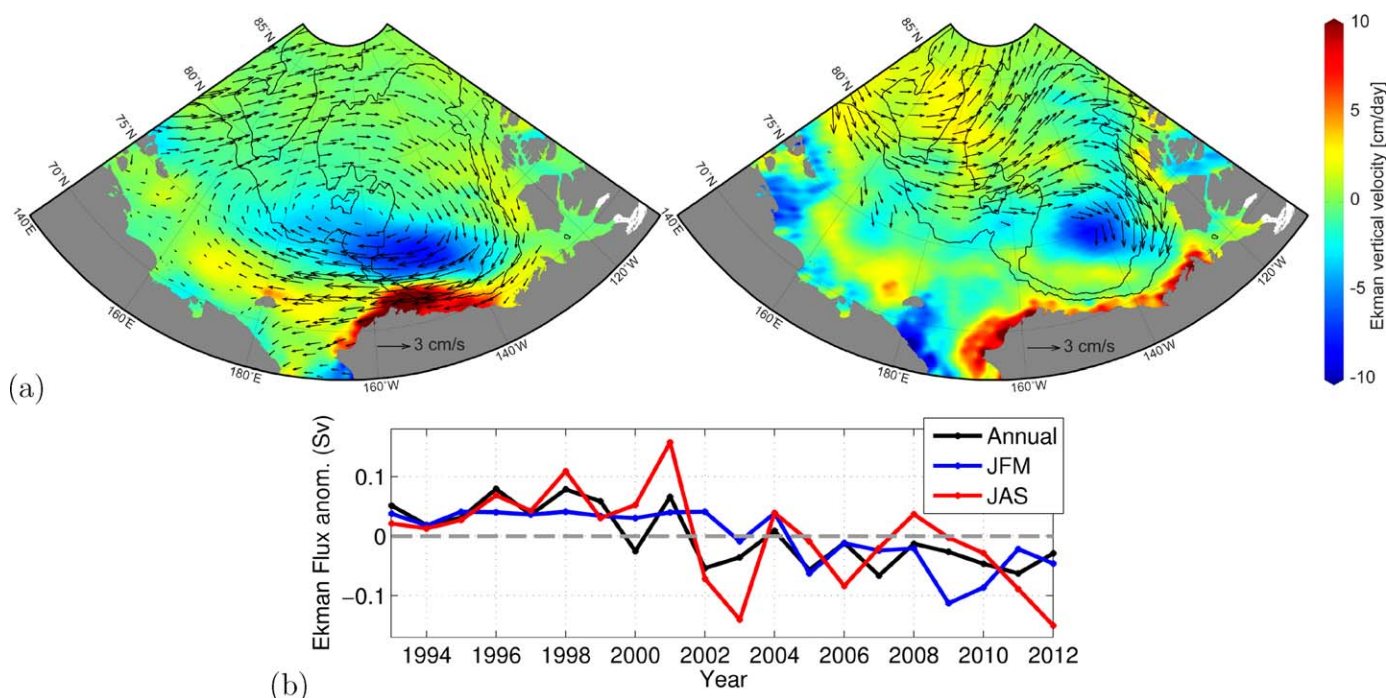Maps of the summer and winter mean distributions of Ekman vertical velocity

Figure 18. (a) Winter (January, February, March) (left) and Summer (July, August, September) (right) mean distributions of Ekman vertical velocity (cm/d, negative is downward) for the period 2003–2012 (sea-ice drift data for 2013 were not available) calculated as described in the text. In both seasons, the strongest downwelling is concentrated in the central Canada Basin (Beaufort Gyre region). Average sea-ice drift vectors are shown. (b) Annual, Summer, and Winter mean Ekman downwelling (Sv) over a region bounded by 120°W–180°W, 70°N–80°N; anomalies from the mean over the time period are plotted (negative values are enhanced downwelling).

(2003–2012) show the strongest region of downward Ekman pumping in the south-central Canada Basin region associated with the strong anticylonic Beaufort Gyre circulation; surrounding regions are characterized by weaker downward pumping (Figure 18). Closer to the coastal regions, Ekman upwelling dominates and transfers fluid from the halocline to the surface where it contributes to water mass transformation in the mixed layer. Ekman pumping has a strong seasonal cycle and month-to-month variability, with weakest values in summer and early fall [*Yang*, 2009; *Proshutinsky et al.*, 2009]. In the two decades preceding 2013, there was an overall increase in summer Ekman downwelling over the entire Canada Basin associated with a transition to a more intense atmospheric anticyclonic circulation regime in the late 1990s (Figure 18b and see *McPhee* [2013] and *Proshutinsky et al.* [2009]). *Proshutinsky et al.* [2009] demonstrate a correlation between increased freshwater content and this enhanced wind stress curl over the Beaufort Gyre.

In 2003–2012, we find only small interannual variability in Ekman pumping with no clear trend. In summer (July, August, September) mean Ekman downwelling is derived over a region of the Chukchi Sea (bounded by 160°W–180°W and 70°N–74°N, consistent with a region having PSW properties at the surface, Figure 19a); similarly small variability is noted in winter, although with mean downwelling about twice as strong as in summer. Between 2003 and 2012, summer-mean subduction in this region is 0.12 ± 0.04 Sv (1 Sv = 10^6 $m^3 s^{-1}$). This rate of about 3×10^{11} $m^3 month^{-1}$ implies that almost half of the PSW layer in the CCB could be renewed over a couple of years (taking the area of the CCB approximately 2×10^5 km^2, and PSW thickness of about 100 m). There is likely also some contribution to subduction from lateral induction. The above ventilation rate estimate simply assumes that all of the subducted water is brought along isopycnals to the CCB and does not flow elsewhere. It nevertheless suggests that changes in PSW characteristics in the CCB in any given year could reflect summer characteristics of PSW outcropping at the surface in the Chukchi Sea that same year (even considering the ∼300 km distance from the region of outcropping to the CCB).

Using the estimates of Ekman downwelling computed here, we can show that the time scales for ventilation are consistent with the surface to interior temperature-salinity mapping illustrated in Figures 15b and 16b. September 2012 indicates Ekman downwelling in the region of the transect shown in Figure 15 of about 2 m/month (∼6–7 cm/d). While the sea-ice drift velocity product [*Fowler et al.*, 2013] is not yet available for
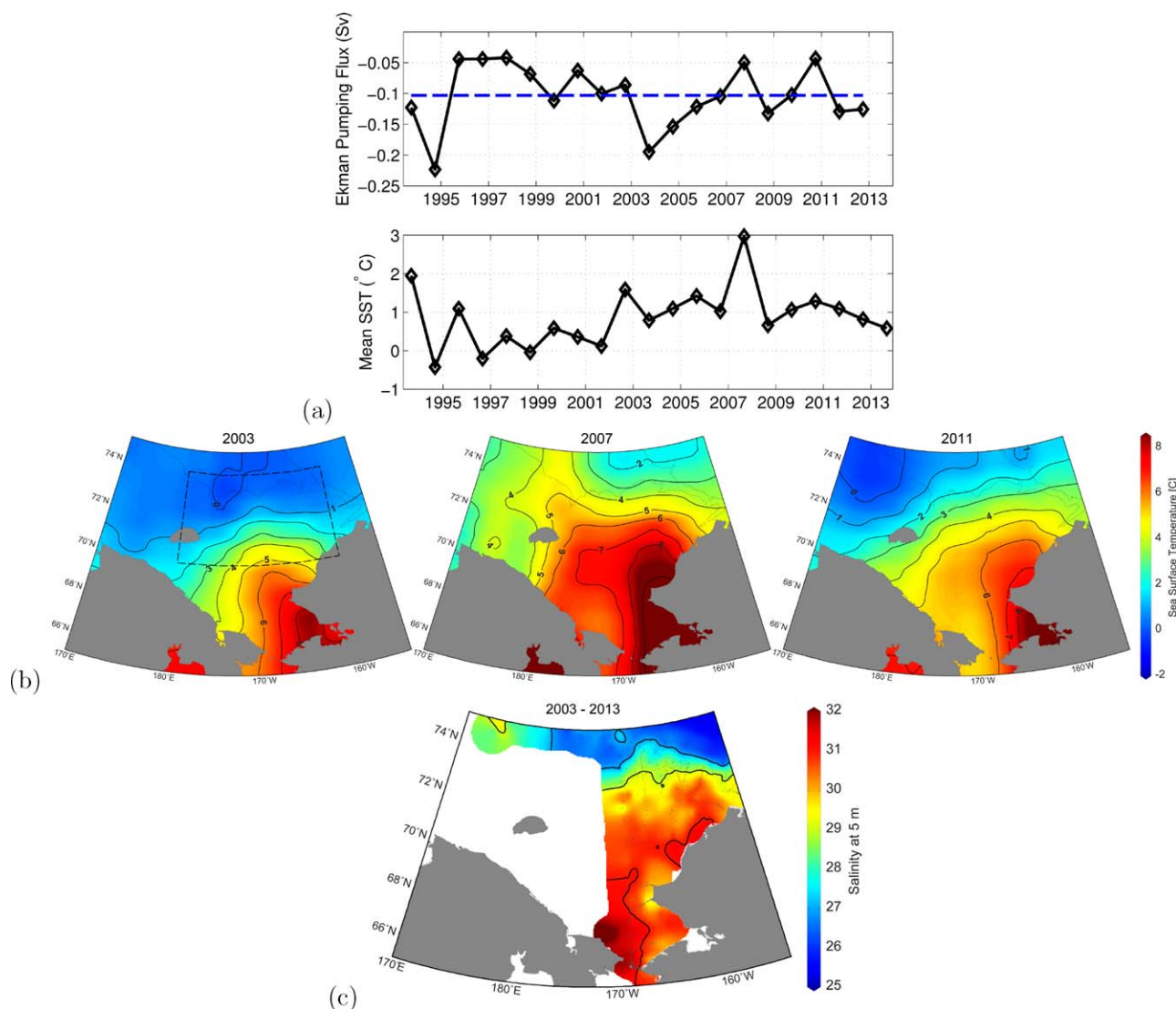
Figure 19. (a) September mean Ekman downwelling (Sv) over a region bounded by 160°W–180°W, 70°N–74°N (dashed line indicates the mean), and September mean sea-surface temperatures (SST) over the same region (NOAA Optimum Interpolation SST V2 [*Reynolds et al.*, 2002]. (b) September mean SST where the dashed line in the left figure indicates the region of interest in Figure 19a; (c) summer salinity (5 m depth) from hydrography archived at the 2013 World Ocean Database (WOD13; www.nodc.noaa.gov/OC5/WOD13/) plus Mirai 2012–2013 measurements, 2003–2013.

2013, computations using the wind-only field in September 2013 (a good representation of Ekman pumping in the region in summer when conditions were ice free) indicates 2 m/month is also an appropriate estimate for Ekman downwelling in the region of the transect shown in Figure 16. This may be enhanced by the lateral transfer of water below the mixed layer base. Estimating the gradient in mixed-layer depth to be about 10 m over 200 km and even a weak flow perpendicular to this of about 1 cm/s, yields about 1 m/month. Estimating a horizontal separation of outcropping PSW isohalines at the surface of about 100 km and $Su \approx 3$ m/month, yields a downwelling flux of about 3×10^5 m^2 month^{-1}. Therefore, for vertical spacing of the same isohalines at the most offshore part of the transects (Figures 15 and 16) of about 10 m, the speed at which water parcels could be ventilated is about 100 km in 3 months. This is sufficiently fast to preserve the mapping of horizontal temperature and salinity structure to the vertical, and likely to be faster with the influence of eddies.

These estimates for penetration of PSW to the interior Canada Basin highlight the importance of changes in source-water properties. In 2007, for example, satellite sea-surface temperatures show anomalously warm temperatures in the Chukchi Sea (Figures 19a and 19b). This is consistent with the anomalously warm ACW

θ_{max} (Figure 6) and submixed layer-averaged temperatures (Figure 7) in the CCB in that year, although with reduced temperatures from those found in the Chukchi, presumably because of some cooling during the transit. Further, if anomalously fresh and warm waters are found in the Chukchi Sea region of outcropping PSW, only the low-salinity portion of the PSW layer is ventilated in summer. Surface salinity measurements are limited in space and time (Figure 19c) but anomalously fresh waters in summer 2007 in the Chukchi would be consistent with a fresher ACW θ_{max} observed at shallower depths in the CCB (Figure 6).

The lateral transition in CCB water mass structure documented in Figures 11–13 is also consistent with changes in properties of the subducting source water in the Chukchi. The spatial/temporal transition in water mass properties indicates subduction not of sBSW, but of ACW. This is consistent with Brugler et al.'s (submitted manuscript, 2014) study showing that under increased easterly winds in recent years, there is a shift from eastward flow of ACW to a flow path that is more to the west and north (Brugler et al., submitted manuscript, 2014). Here the ACW is available for subduction from the Chukchi Sea into the interior basin. Of course in addition to the importance of source-water properties, the mechanism outlined here also demonstrates the importance of shifts in the distribution and intensity of Ekman pumping in setting the PSW property distribution in the interior CCB, which has strong seasonal and interannual variability. Expansion and contraction of the gyre circulation leads to position shifts of the surface front. Isopycnals also outcrop at the northern boundary of the gyre and a strong downward pumping in this region could dominate over the pumping of southern waters to the interior.

Seasonal variability in subduction rates coupled with seasonal variability of surface properties in the region of PSW isopycnal outcropping is key to the presence of a warm PSW layer found year round in the CCB. In summer, influences from river runoff and sea-ice melt freshen the surface waters in the Chukchi and the outcropping isohalines are fresher there than in winter (when surface salinity is additionally increased by sea-ice growth). This leads to shallower (fresher and warmer) waters being ventilated in summer, and deeper (saltier and cooler) waters being ventilated in winter. The basic ventilation process is demonstrated numerically in the next section.

The goal of the modeling is to demonstrate the general result of the combined forcing of Pacific Water inflow and winds. We employ a model that includes only the dynamical influences of idealized winds and inflowing Pacific Waters; sea-ice and buoyancy forcing (associated with surface heating, cooling and sea ice transformations) are neglected. While the actual flow field will depend on the characteristics of sea-ice, surface buoyancy forcing, the exact wind field, river inflows and other complexities, the model results show fundamentally how the large-scale wind forcing drives Pacific Water pathways to the interior by subduction and flow along geostrophic contours.

4.3. Idealized Model Results

We employ the Institute of Computational Mathematics and Mathematical Geophysics (ICMMG) 3-D hydrostatic ocean model to investigate Pacific Water dynamics in the Canada Basin. The southern boundary of the model domain is Bering Strait in the Pacific sector and 20°S in the Atlantic Ocean, with all major Arctic straits included. In the Arctic Ocean region, model horizontal grid resolution is about 25 km, with 38 levels in the vertical (5 m increments in the upper 20 m, and 20–25 m vertical resolution through the halocline). Model bathymetry is from the 2.5 km International Bathymetric Chart of the Arctic Ocean (IBCAO) [*Jakobsson et al.*, 2012]. Horizontal mixing is represented by a Laplacian diffusivity of 10^7 cm^2/s, and vertical diffusion is treated as in *Bryan and Lewis* [1979] with vertical diffusivity 0.05 cm^2/s; see *Golubeva and Platov* [2007, 2009] for full model details.

We conducted experiments both in the absence of wind forcing and with wind forcing specified by an idealized sea-level pressure distribution with a central high at 147°W, 77°N (Figure 20). This sea-level pressure distribution is used to compute a geostrophic wind, which is then converted to a surface wind stress following *Proshutinsky and Johnson* [1997]. The position of the central high corresponds to the climatological Arctic High center. This wind distribution yields a maximum Ekman pumping (computed from the wind stress curl) of about 2 cm/d around the core of the high and a maximum upwelling of about 3 cm/d at the Alaskan/Beaufort coastline. Idealized initial conditions with horizontally uniform salinity and vertically stratified salinity corresponding to typical conditions (i.e., consistent with observations presented here) in the Canadian Basin sector were prescribed in all experiments (Figure 21, bottom). There was no sea ice, and no surface buoyancy fluxes were applied in the experiments. Water temperature was prescribed to be uniform
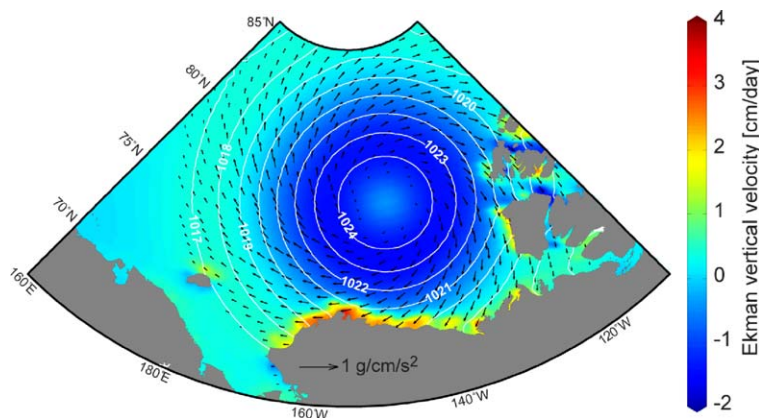
Figure 20. Idealized wind forcing prescribed in the model and Ekman vertical velocities (cm/d) computed from the wind stress curl at the ocean surface (sea-ice is not included in any of our model experiments here). Positive indicates wind forcing responsible for upwelling and negative, downwelling. Arrows depict strength and direction of wind stresses (g cm^{-1} s^{-2}) generated by an idealized Arctic High sea level pressure (white concentric isolines, hPa) centered over its climatic 1948-present location. Note that maximum downwelling is observed not in the center of the Arctic High but at some distance from the center where wind stress curl is most negative.

($-1°$C) in both the vertical and the horizontal; at typical temperatures of these regions the influence of temperature changes on density can be neglected. At the model domain's southern boundary ($20°$S), boundary conditions allowed free advection out of the model domain such as to maintain the initial salinity distribution in the case of water advection directed inward. No surface restoring was applied. A constant barotropic transport into the Arctic Ocean of 0.8 Sv (with v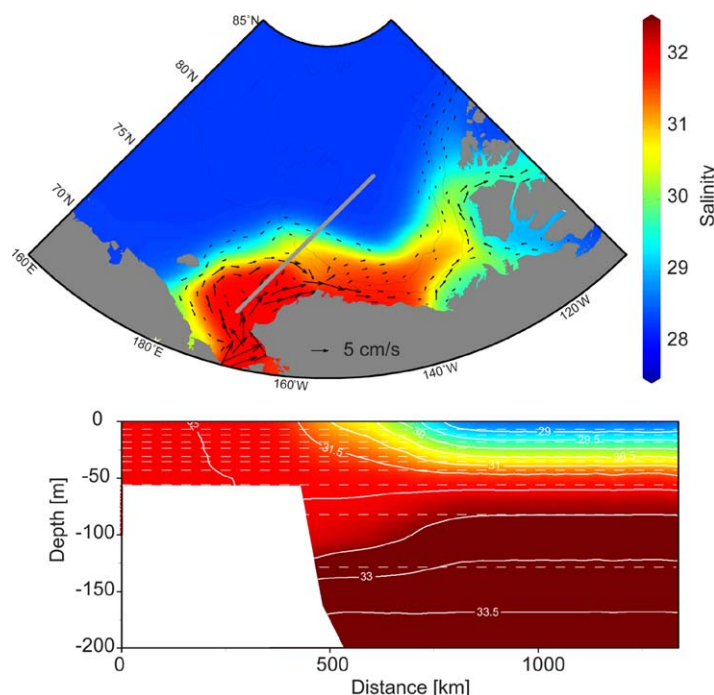ertically uniform salinity of 32) through Bering Strait was also imposed. We present results for a case with only Bering Strait inflow and no wind forcing (Figure 21), with only the idealized wind forcing and no Bering Strait inflow (Figure 22), and with both Bering Strait inflow and idealized wind forcing (Figure 23).

Pacific Water pathways originating from Bering Strait were assessed by examining the duration of time (particle hours) that particles occupied a given model grid cell. Every 5 days, six passive particles were released in Bering Strait at 0, 5, 10, 15, 20, and 30 m depth and their coordinates calculated from the simulated 3-D velocity fields over 48 months. After this time, the salinity structure and wind-driven/buoyancy currents are well established while mixing processes (numerical and physical) have not dominated the model solution. At run times longer than 48 months, frontal zones tend to weaken
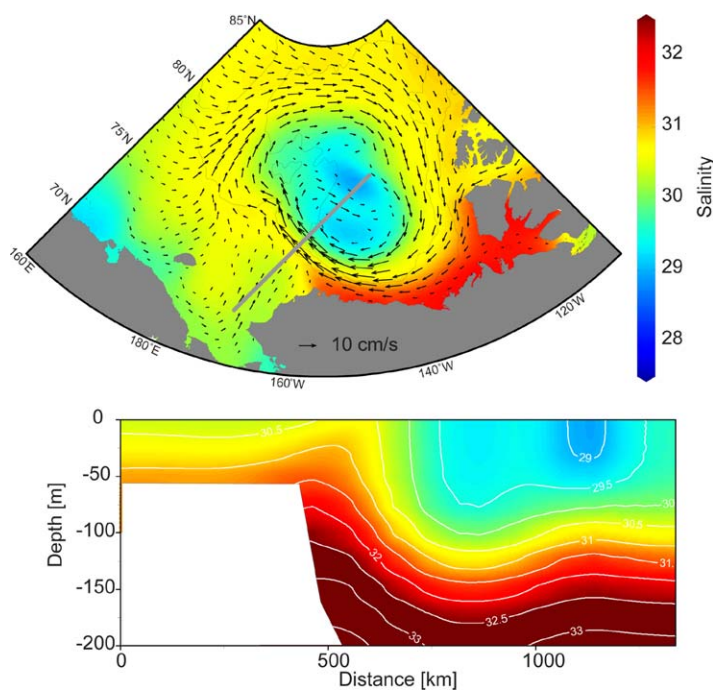

Figure 21. Results of model experiment without wind forcing. (top) Map of surface salinity and currents after 48 months of simulation. (bottom) Salinity-depth section (along the gray line in the top map) after 48 months; the dashed lines show the initial horizontally uniform salinity stratification (corresponding to each of the solid contours also shown: the shallowest dashed line is $S = 29$, with contour spacing of 0.5). Pacific Water with salinity $S = 32$ flows in via Bering Strait and is responsible for the formation of a frontal zone between Pacific waters and relatively fresh surface waters of the upper Arctic Ocean. This is in a good qualitative agreement with Figures 14 and 19c where salinity distributions are shown based on observations.

and the entire upper ocean becomes saltier as a result of vertical mixing. Analysis of particle concentrations (particle hours) in each experiment (after 48 h) allows us to understand differences in Pacific Water circulation patterns with and without wind forcing.

In the absence of wind forcing, the Pacific Water flows northward and veers east to flow as a boundary current along the Alaska-Beaufort coast in the Chukchi Sea and Canada Basin; isohaline displacements are confined to the coastal regions (Figure 21). Two main topographically steered branches are clear in the surface flow field over the shallow Chukchi Sea [e.g., see *Weingartner et al.*, 2005]. At the surface, the density of the inflowing Pacific Water exceeds that of the inte-

Figure 22. As in Figure 21 but for an experiment with only idealized wind forcing (Figure 20) and no Bering Strait inflow. The wind forcing drives a freshwater convergence in the Beaufort Gyre region.

rior surface Arctic water by about 2.4 kg m^{-3}. The strongest sinking of the inflowing dense water is evident at the shelf-slope boundary as the inflowing water sinks to its level of neutral buoyancy (Figures 24 and 25a) [see, e.g., *Aagaard and Roach*, 1990; *Pickart et al.*, 2005]. Downwelling is effectively confined to this region and particle tracers show little penetration to the interior. The inflowing Pacific Water generates an

intense frontal zone between salty inflowing waters and relatively fresh interior surface Arctic water (Figure 21). In the model, however, the strength of this front decreases over time as the entire region becomes increasingly salty due to mixing with the inflowing salty water. The neutral buoyancy level of the inflowing layer shoals over time.
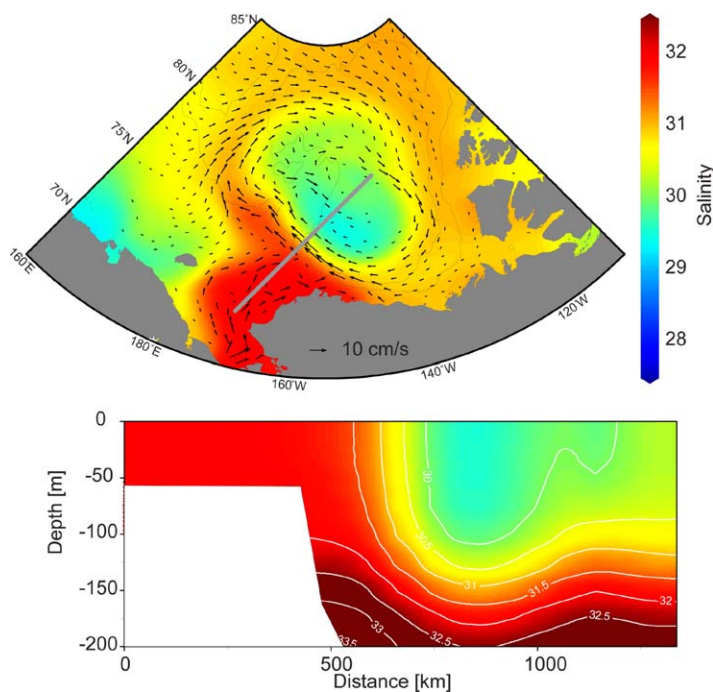
When the large-scale idealized wind forcing is applied in the absence of flow through Bering Strait (i.e., a closed strait), winds drive a flux of surface water from the Bering Strait region into the Canada Basin (Figure 22); this suggests how the intensification of the anticyclonic circulation in recent years could play a role in the recent increase in Bering Strait
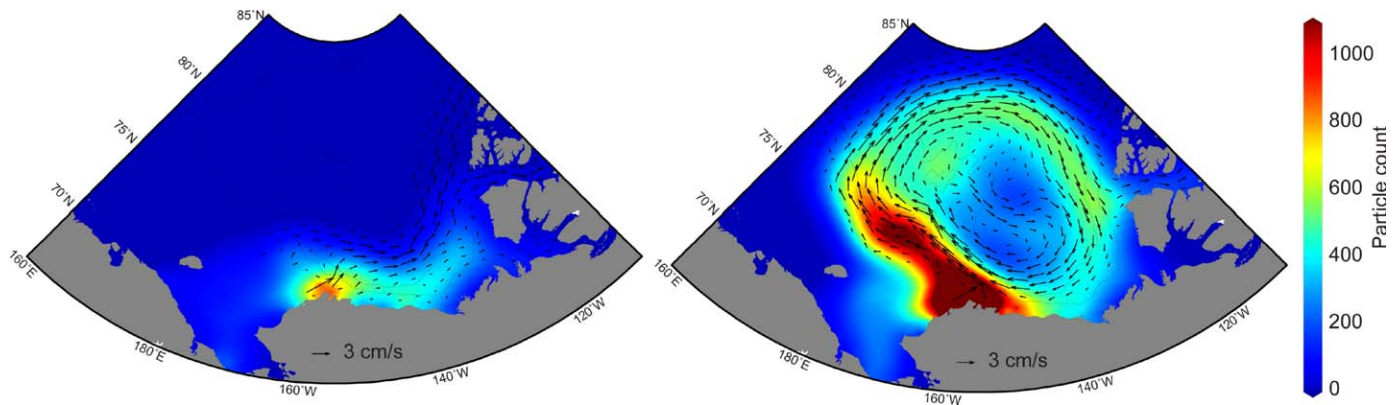

Figure 23. As in Figure 21 but for an experiment with both Bering Strait inflow and idealized wind forcing shown in Figure 20.

Figure 24. Results of model experiments (after 48 months) with Bering Strait inflow showing colored contours of water tracer particle hours (see text) in the (left) absence of wind forcing and (right) presence of idealized wind forcing shown in Figure 20; colors show particle concentration integrated between 50 and 150 m and arrows show currents at 75 m depth.

transport observed by *Woodgate et al.* [2012]. In this case there is no eastward flow along the coast of Alaska/Canada. The wind-forced circulation is distinguished by a strong, anticyclonic Beaufort Gyre and an accumulation of fresh surface water here by converging Ekman transport (Figures 22 and 24). With both wind forcing and a prescribed flow through Bering Strait, the surface front set up by the Pacific Water inflow is intensified (Figure 23). The strongest sinking is again associated with relatively dense Pacific Water sinking to its level of neutral buoyancy along the Chukchi shelf slope (Figures 24 and 25a). In this case, however, the anticyclonic wind forcing drives additional downwelling over a large region of the Canada Basin,
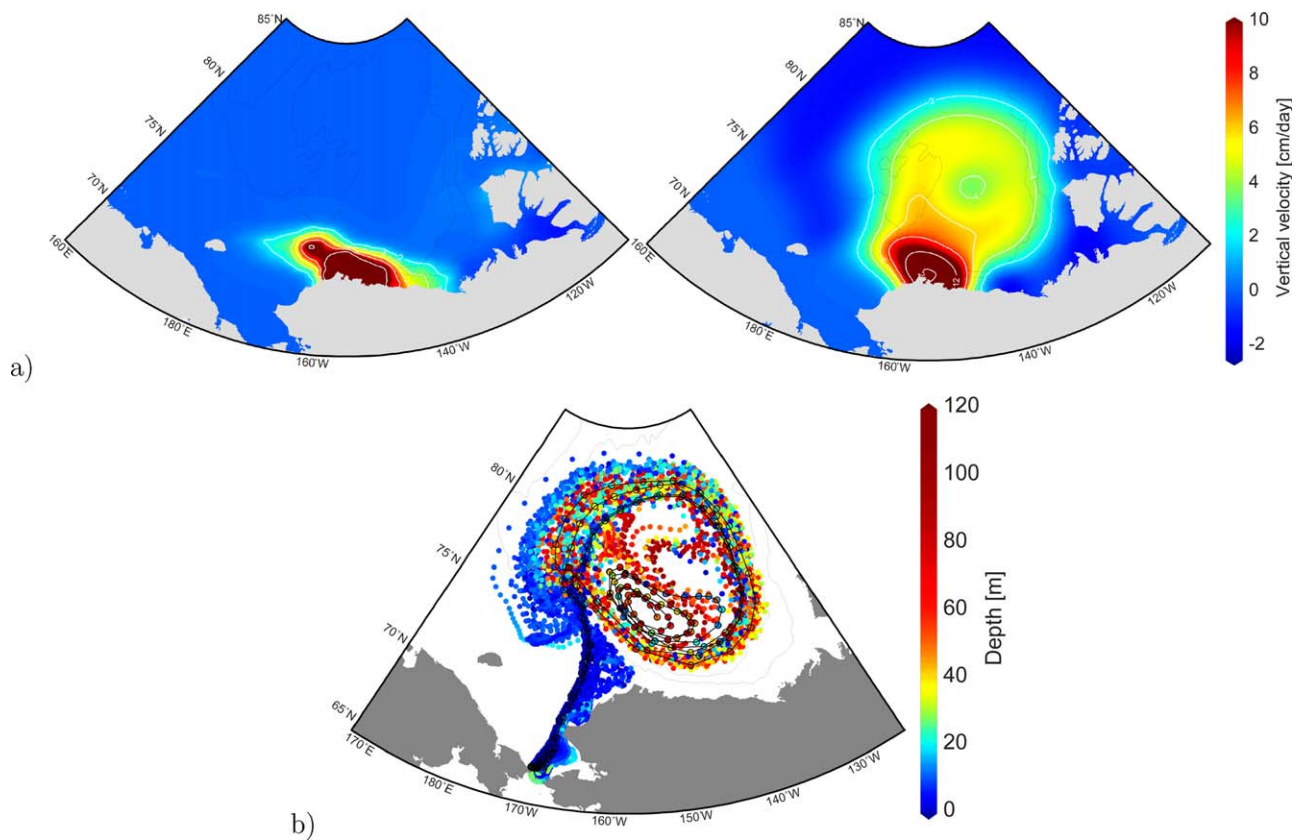

Figure 25. (a) Results of model experiments (after 48 months) with Bering Strait inflow showing mean vertical velocity at 50 m depth (left) in the absence of wind forcing and (right) in the presence of idealized wind forcing. Note that in this plot positive vertical velocity is downward. (b) Particle trajectory tracks (after 48 months) for particles released at the start of the wind-forced experiment with a closed Bering Strait.

particularly at the periphery of the gyre corresponding to outcropping isopycnals, as well as upwelling along the continental slope and coastlines (Figures 20 and 23). Water is subducted while being swept along geostrophic contours such that water pathways along isopycnals approximate a helical structure (Figure 25b). Although there are many complicating factors (e.g., the influence of sea ice) not represented in the model, results show water parcels are subducted and swept toward the interior at rates consistent with the estimates in section 4.2: of the order of a hundred kilometers over a few months (the magnitude of wind forcing is appropriate for typical annual-average values). Horizontal salinity (density) gradients are intensified at the frontal zone by convergence of fresh surface waters accumulated by Ekman transport to the center of the Beaufort Gyre, and the salinification of surface Chukchi Sea water driven by upwelling close to the coast. Downwelling is enhanced in the frontal region (further west than in the case of no winds) where it is responsible for transferring water along isopycnals into the interior basin (Figures 24 and 25).

The anticyclonic wind forcing drives a clear steepening of isohalines (isopycnals) and a deepening of the mixed layer on either side of the front (Figure 23). The strong isopycnal displacements associated with spin-up of the Beaufort Gyre circulation leads to increased Pacific Water layer thickness and enhanced ventilation of this layer. Although not captured in this model configuration, the deeper front and steeper isopycnal slopes forced by winds also increases the likelihood of baroclinic instability and eddy-driven transfer of water masses along isopycnals into the interior (model horizontal grid resolution is larger than the first baroclinic Rossby deformation radius in the region [see *Nurser and Bacon*, 2013]).

5. Discussion and Summary

We have analyzed the constituent PSW masses in the CCB to show that salinity ranges of $29 < S < 32.2$ for ACW and $32.2 < S < 33$ for sBSW are appropriate for the years 2003–2013. The most important difference here to past accepted ranges is the significant freshening of the ACW. Because ACW and sBSW are fundamentally characterized by their salinities, ensuring the appropriate salinity ranges are examined is imperative for any study of the Pacific Water. For example, *Bourgain and Gascard* [2012] would have reached different conclusions for the temperature variability of ACW by considering a salinity range that included values fresher than $S = 31$; *Jackson et al.* [2011] find PSW fresher than this in 2008, and we have found that the recent warm temperatures of the PSW are associated with fresh layers with θ_{max} having $S < 31$. The accurate identification of PSW is also essential to differentiate them from overlying water masses in the CCB that are modified in place by buoyancy fluxes and stronger mixing than at depth.

The interannual variability in the ACW θ_{max} over 2003–2013 in the CCB is as large as 1°C, with warming of the ACW θ_{max} broadly congruent with freshening. ACW θ_{max} temperature and salinity display similar interannual variability and trends as layer-averaged temperature and salinity and PSW heat and freshwater content. No apparent seasonal variability of the PSW was observed in the CCB. While it is likely that different halocline depths are ventilated in different seasons, only extensive year-round hydrographic measurements in the Chukchi Sea will allow us to examine this further. Shoaling of the ACW θ_{max} is generally related to a freshening, although interannual variability in surface salinity in the Chukchi Sea is difficult to quantify, so it is unclear how this relates to Chukchi Sea properties. The deepening of the deep isohaline bound on the PSW in the CCB is consistent with intensification of the BG circulation in the recent decade.

We have shown a mapping of horizontal temperature-salinity structure to vertical structure in transects from the Chukchi Sea to the deep Canada Basin, consistent with the CCB halocline being ventilated by subduction of surface Chukchi Sea water. The properties at the Chukchi Sea surface in summer (set by buoyancy fluxes, the properties of the inflowing Pacific Water, and contributions from surface wind-driven flows from the basin margins) set the temperature-salinity properties of PSW in the interior CCB, although with some property modification by weak mixing of the subducted waters. Unusually warm temperatures in the CCB (e.g., in 2007) appear to be linked to warm anomalies in the Chukchi Sea.

Intensified subduction rates (due to increased Ekman pumping) can have significant consequences during times when Chukchi Sea surface waters are anomalously warm; this is because the additional heat can be archived in the CCB PSW layer where it can later influence the surface-ocean heat budget and sea ice. Note also that when fresher source water is available for subduction [see, e.g., *Morison et al.*, 2012], increased freshwater content can arise in the CCB even when the strength of downward Ekman pumping does not increase. There is significant complexity in understanding upper-halocline properties because they involve

a combination of the strongly seasonally varying surface Chukchi Sea waters and the wind stress curl forcing which shows strong variations spatially, seasonally and interannually. For example, we have shown that the presence or absence of sBSW in the CCB (which relies on Ekman pumping and properties of outcropping isopycnals) influences integrated freshwater content in this region. Freshwater content is largest when ACW dominates over sBSW. This study highlights the need for additional data tracking the seasonal evolution and distribution of water-column properties in the Chukchi Sea analogous to the ITP data that exist in the CCB. It also underlines the need for detailed information on mixed-layer depth and horizontal velocity fields to quantify lateral induction of outcropping water masses, and understand how variability in atmospheric forcing and sea-ice cover is transferred to the interior Arctic Ocean.

Finally, eddies are likely to play a significant role in transferring water along isopycnals in the interior. For example, *Spall et al.* [2008] have shown how mesoscale eddies are an important transport mechanism for flux of Pacific Water from the shelf/slope regions offshore into the interior Canada Basin. Frontal instabilities are also associated with subduction [e.g., *Spall*, 1995; *Timmermans et al.*, 2008; *Thomas and Joyce*, 2010]. Further studies are required to examine the role of mesoscale and submesoscale eddies and frontal instabilities in modifying the subduction rate of PSW into the halocline.

References

Aagaard, K., and A. T. Roach (1990), Arctic ocean-shelf exchange: Measurements in Barrow Canyon, *J. Geophys. Res.*, *95*(C10), 18,163–18,175.

Bourgain, P., and J. C. Gascard (2012), The Atlantic and summer Pacific waters variability in the Arctic Ocean from 1997 to 2008, *Geophys. Res. Lett.*, *39*, L05603, doi:10.1029/2012GL051045.

Bryan, K., and L. J. Lewis (1979), A water mass model of the World Ocean, *J. Geophys. Res.*, *84*(C5), 2503–2517, doi:10.1029/JC084iC05p02503.

Carmack, E., and H. Melling (2011), Cryosphere: Warmth from the deep, *Nat. Geosci.*, *4*, 7–8, doi:10.1038/ngeo1044.

Carpenter, J. R., and M.-L. Timmermans (2012), Deep mesoscale eddies in the Canada Basin, Arctic Ocean, *Geophys. Res. Lett.*, *39*, L20602, doi:10.1029/2012GL053025.

Clement Kinney, J., W. Maslowski, Y. Aksenov, B. de Cuevas, J. Jakacki, A. Nguyen, R. Osinski, M. Steele, R. A. Woodgate, and J. Zhang (2014), On the flow through Bering Strait: A synthesis of model results and observations in *The Pacific Arctic Region: Ecosystem Status and Trends in a Rapidly Changing Environment*, chap. 7, edited by J. M. Grebmeier and W. Maslowski, pp. 167–191, Springer, doi:10.1007/978-94-017-8863-24.

Coachman, L. K., and C. A. Barnes (1961), The contribution of Bering Sea Water to the Arctic Ocean, *Arctic*, *14*(3), 147–161.

Coachman, L. R., K. Aagaard, and R. B. Tripp (1975), *Bering Strait: The Regional Physical Oceanography*, 172 p., Univ. of Wash. Press, Seattle, Wash.

Falkner, K. K., M. Steele, R. A. Woodgate, J. H. Swift, K. Aagaard, and J. Morison (2005), Dissolved oxygen extrema in the Arctic Ocean halocline from the North Pole to the Lincoln Sea, *Deep Sea Res., Part I*, *52*(7), 1138–1154.

Fedorova, Z. P., and Z. S. Yankina (1963), Supply of Pacific Water through the northern Bering Strait, *Trudy AANII*, *3*, 21–44.

Fowler, C., W. Emery, and M. Tschudi (2013), *Polar Pathfinder Daily 25 km EASE-Grid Sea Ice Motion Vectors*, Version 2, Natl. Snow and Ice Data Cent., Boulder, Colo.

Golubeva, E. N., and G. A. Platov (2007), On improving the simulation of Atlantic water circulation in the Arctic Ocean, *J. Geophys. Res.*, *112*, C04S05, doi:10.1029/2006JC003734.

Golubeva, E. N., and G. A. Platov (2009), Numerical modeling of the Arctic Ocean ice system response to variations in the atmospheric circulation from 1948 to 2007, *Izv. Atmos. Oceanic Phys.*, *45*(1), 137–151.

Iselin, C. O. D. (1939), The influence of vertical and lateral turbulence on the characteristics of the waters at mid-depths, *Trans. AGU*, *20*, 414–417.

Jackson, J. M., E. C. Carmack, F. A. McLaughlin, S. E. Allen, and R. G. Ingram (2010), Identification, characterization, and change of the near-surface temperature maximum in the Canada Basin, 1993–2008, *J. Geophys. Res.*, *115*, C05021, doi:10.1029/2009JC005265.

Jackson, J. M., S. E. Allen, F. A. McLaughlin, R. A. Woodgate, and E. C. Carmack (2011), Changes to the near-surface waters in the Canada Basin, Arctic Ocean from 19932009: A basin in transition, *J. Geophys. Res.*, *116*, C10008, doi:10.1029/2011JC007069.

Jakobsson, M., et al. (2012), The International Bathymetric Chart of the Arctic Ocean (IBCAO) Version 3.0, *Geophys. Res. Lett.*, *39*, L12609, doi:10.1029/2012GL052219.

Krishfield, R., J. Toole, A. Proshutinsky, and M.-L. Timmermans (2008), Automated Ice-Tethered Profilers for seawater observations under pack ice in all seasons, *J. Atmos. Oceanic Technol.*, *25*, 2091–2095.

Kwok, R., and J. Morison (2011), Dynamic topography of the ice-covered Arctic Ocean from ICESat, *Geophys. Res. Lett.*, *38*, L02501, doi:10.1029/2010GL046063.

Marshall, D. (1997), Subduction of water masses in an eddying ocean, *J. Mar. Res.*, *55*(2), 201–222.

McPhee, M. G. (2013), Intensification of geostrophic currents in the Canada Basin, Arctic Ocean, *J. Clim.*, *26*(10), 3130–3138.

McPhee, M. G., T. P. Stanton, J. H. Morison, and D. G. Martinson (1998), Freshening of the upper ocean in the Arctic: Is perennial sea ice disappearing?, *Geophys. Res. Lett.*, *25*(10), 1729–1732.

Morison, J., R. Kwok, C. Peralta-Ferriz, M. Alkire, I. Rigor, R. Andersen, and M. Steele (2012), Changing Arctic Ocean freshwater pathways, *Nature*, *481*(7379), 66–70.

Newton, R., P. Schlosser, R. Mortlock, J. Swift, and R. MacDonald (2013), Canadian Basin freshwater sources and changes: Results from the 2005 Arctic Ocean Section, *J. Geophys. Res. Oceans*, *118*, 2133–2154, doi:10.1002/jgrc.20101.

Nikolopoulos, A., R. S. Pickart, P. S. Fratantoni, K. Shimada, D. J. Torres, and E. P. Jones (2009), The western Arctic boundary current at 152°W: Structure, variability, and transport, *Deep Sea Res., Part II*, *56*(17), 1164–1181.

Nurser, A. G., and J. C. Marshall (1991), On the relationship between subduction rates and diabatic forcing of the mixed layer, *J. Phys. Oceanogr.*, *21*(12), 1793–1802.

Nurser, A. J. G., and S. Bacon (2013), Eddy length scales and the Rossby radius in the Arctic Ocean, *Ocean Sci. Discuss.*, *10*, 1807–1831, doi: 10.5194/osd-10-1807-2013.

Perovich, D. K., J. A. Richter-Menge, K. F. Jones, and B. Light (2008), Sunlight, water, and ice: Extreme Arctic sea ice melt during the summer of 2007, *Geophys. Res. Lett.*, *35*, L11501, doi:10.1029/2008GL034007.

Pickart, R. S., T. J. Weingartner, L. J. Pratt, S. Zimmermann, and D. J. Torres (2005), Flow of winter-transformed Pacific water into the Western Arctic, *Deep Sea Res., Part II*, *52*(24), 3175–3198.

Pickart, R. S., L. J. Pratt, D. J. Torres, T. E. Whitledge, A. Y. Proshutinsky, K. Aagaard, T. A. Agnew, G. W. K. Moore, and H. J. Dail (2009), Evolution and dynamics of the flow through Herald Canyon in the western Chukchi Sea, *Deep Sea Res., Part II*, *57*(1-2), 5–26, doi:10.1016/j.dsr2.2009.08.002.

Proshutinsky, A., R. Krishfield, M.-L. Timmermans, J. Toole, E. Carmack, F. McLaughlin, W. J. Williams, S. Zimmermann, M. Itoh, and K. Shimada (2009), Beaufort Gyre freshwater reservoir: State and variability from observations, *J. Geophys. Res.*, *114*, C00A10, doi:10.1029/2008JC005104.

Proshutinsky, A., et al. (2011), The Arctic Ocean [in "State of the Climate in 2010"], *Bull. Am. Meteorol. Soc.*, *92*, S145–S148.

Proshutinsky, A., et al. (2012), The Arctic Ocean [in "State of the Climate in 2011"], *Bull. Am. Meteorol. Soc.*, *93*, S57–S92.

Proshutinsky, A. Y., and M. A. Johnson (1997), Two circulation regimes of the wind-driven Arctic Ocean, *J. Geophys. Res.*, *102*(C6), 12,493–12,514.

Proshutinsky, A. Yu. (1986), *On the Problem of Calculating the Storm Surge Fluctuations of Sea Level and Water Circulation in the Chukchi Sea*, *Sov. Meteorol. Gidrol.*, vol. 1, pp. 54–61, Allerton Press, N. Y.

Reynolds, R. W., N. A. Rayner, T. M. Smith, D. C. Stokes, and W. Wang (2002), An improved in situ and satellite SST analysis for climate, *J. Clim.*, *15*(13), 1609–1625.

Shimada, K., E. C. Carmack, K. Hatakeyama, and T. Takizawa (2001), Varieties of shallow temperature maximum waters in the Western Canadian Basin of the Arctic Ocean, *Geophys. Res. Lett.*, *28*(18), 3441–3444, doi:10.1029/2001GL013168.

Shimada, K., T. Kamoshida, M. Itoh, S. Nishino, E. Carmack, F. McLaughlin, S. Zimmermann, and A. Proshutinsky (2006), Pacific Ocean inflow: Influence on catastrophic reduction of sea ice cover in the Arctic Ocean, *Geophys. Res. Lett.*, *33*, L08605, doi:10.1029/2005GL025624.

Spall, M. A. (1995), Frontogenesis, subduction, and cross-front exchange at upper ocean fronts, *J. Geophys. Res.*, *100*(C2), 2543–2557.

Spall, M. A. (2007), Circulation and water mass transformation in a model of the Chukchi Sea, *J. Geophys. Res.*, *112*, C05025, doi:10.1029/2005JC003364.

Spall, M. A., R. S. Pickart, P. S. Fratantoni, and A. J. Plueddemann (2008), Western Arctic shelfbreak eddies: Formation and transport, *J. Phys. Oceanogr.*, *38*(8), 1644–1668.

Steele, M., J. Morison, W. Ermold, I. Rigor, M. Ortmeyer, and K. Shimada (2004), Circulation of summer Pacific halocline water in the Arctic Ocean, *J. Geophys. Res.*, *109*, C02027, doi:10.1029/2003JC002009.

Stommel, H. (1979), Determination of water mass properties of water pumped down from the Ekman layer to the geostrophic flow below, *Proc. Natl. Acad. Sci. U. S. A.*, *76*, 3051–3055.

Thomas, L. N. (2008), Formation of intrathermocline eddies at ocean fronts by wind-driven destruction of potential vorticity, *Dyn. Atmos. Oceans*, *45*(3), 252–273.

Thomas, L. N., and T. M. Joyce (2010), Subduction on the Northern and Southern Flanks of the Gulf Stream, *J. Phys. Oceanogr.*, *40*(2), 429–438.

Thompson, D. W., and J. M. Wallace (1998), The Arctic Oscillation signature in the wintertime geopotential height and temperature fields, *Geophys. Res. Lett.*, *25*(9), 1297–1300.

Timmermans, M.-L., J. Toole, A. Proshutinsky, R. Krishfield, and A. Plueddemann (2008), Eddies in the Canada Basin, Arctic Ocean, observed from Ice-Tethered Profilers, *J. Phys. Oceanogr.*, *38*(1), 133–145.

Timmermans, M.-L., R. Krishfield, S. Laney, and J. Toole (2010), Ice-Tethered Profiler measurements of dissolved oxygen under permanent ice cover in the Arctic Ocean, *J. Atmos. Oceanic Technol.*, *27*, 1936–1949, doi:10.1175/2010JTECHO772.1.

Timmermans, M.-L., et al. (2013), [The Arctic] Ocean temperature and salinity [in "State of the Climate in 2012"], *Bull. Am. Meteorol. Soc.*, *94*(8), S128–S130.

Timmermans, M.-L., et al. (2014), [The Arctic] Ocean temperature and salinity [in "State of the Climate in 2013"], Bull. Am. Meteorol. Soc., *95*, S128–S132.

Toole, J., M.-L. Timmermans, D. Perovich, R. Krishfield, A. Proshutinsky, and J. Richter-Menge (2010), Influences of the ocean surface mixed layer and thermohaline stratification on Arctic sea ice in the central Canada Basin, *J. Geophys. Res.*, *115*, C10018, doi:10.1029/2009JC005660.

Toole, J. M., R. A. Krishfield, M.-L. Timmermans, and A. Proshutinsky (2011), The Ice-Tethered Profiler: Argo of the Arctic, *Oceanography*, *24*(3), 126–135, doi:10.5670/oceanog.2011.64.

von Appen, W.-J., and R. S. Pickart (2012), Two configurations of the Western Arctic shelfbreak current in summer, *J. Phys. Oceanogr.*, *42*, 329–351, doi:10.1175/JPO-D-11-026.1.

Watanabe, E. (2011), Beaufort shelfbreak eddies and shelf-basin exchange of Pacific summer water in the western Arctic Ocean detected by satellite and modeling analyses, *J. Geophys. Res.*, *116*, C08034, doi:10.1029/2010JC006259.

Weingartner, T., K. Aagaard, R. Woodgate, S. Danielson, Y. Sasaki, and D. Cavalieri (2005), Circulation on the north central Chukchi Sea shelf, *Deep Sea Res., Part II*, *52*, 3150–3174, doi:10.1016/j.dsr2.2005.10.015.

Winsor, P., and D. C. Chapman (2004), Pathways of Pacific water across the Chukchi Sea: A numerical model study, *J. Geophys. Res.*, *109*, C03002, doi:10.1029/2003JC001962.

Woodgate, R. A., K. Aagaard, and T. J. Weingartner (2005), A year in the physical oceanography of the Chukchi Sea: Moored measurements from autumn 1990–1991, *Deep Sea Res., Part II*, *52*, 3116–3149, doi:10.1016/j.dsr2.2005.10.016.

Woodgate, R. A., T. Weingartner, and R. Lindsay (2010), The 2007 Bering Strait oceanic heat flux and anomalous Arctic sea-ice retreat, *Geophys. Res. Lett.*, *37*, L01602, doi:10.1029/2009GL041621.

Woodgate, R. A., T. Weingartner, and R. Lindsay (2012), Observed increases in Bering Strait oceanic fluxes from the Pacific to the Arctic from 2001 to 2011 and their impacts on the Arctic Ocean water column, *Geophys. Res. Lett.*, *39*, L24603, doi:10.1029/2012GL054092.

Woods, J. D. (1985), *The Physics of Thermocline Ventilation, Elsevier Oceanogr. Ser.*, vol. 40, pp. 543–590, Elsevier, Amsterdam.

Yang, J. (2006), The seasonal variability of the Arctic Ocean Ekman transport and its role in the mixed layer heat and salt fluxes, *J. Clim.*, *19*(20), 5366–5387.

Yang, J. (2009), Seasonal and interannual variability of downwelling in the Beaufort Sea, *J. Geophys. Res.*, *114*, C00A14, doi:10.1029/2008JC005084.